

# Global seismic energy scaling relationships based on the type of faulting.

Quetzalcoatl Rodríguez-Pérez<sup>1</sup>, F. Ramón Zúñiga<sup>2</sup>

<sup>1</sup> Dirección de Desarrollo Científico, Dirección de Cátedras, Consejo Nacional de Ciencia y Tecnología, Mexico City, Mexico.

<sup>2</sup> Centro de Geociencias, Universidad Nacional Autónoma de México, Juriquilla, Querétaro, Mexico.

Correspondence: Quetzalcoatl Rodríguez-Pérez ([quetza@geociencias.unam.mx](mailto:quetza@geociencias.unam.mx))

**Abstract.** We derived scaling relationships for different seismic energy metrics for earthquakes around the globe with  $M_w > 6.0$  from 1990 to 2022. The seismic energy estimations were derived with two methodologies, the first based on the velocity flux integration and the second based on finite-fault models. In the first case, we analyzed 3331 reported seismic energies derived by integrating far-field waveforms. In the latter methodology, we used the total moment rate functions and the approximation of the overdamped dynamics to quantify seismic energy from 231 finite-fault models ( $E_{mrt}$  and  $E_O$ ,  $E_U$ , respectively). Both methodologies provide compatible energy estimates. The radiated seismic energies estimated from the slip models and integration of velocity records are also compared for different types of focal mechanisms (SS, N-SS, R-SS, SS-N, SS-R, N, R), and then used to derive converting scaling relations among the different energy types. Additionally, the behavior of radiated seismic energy ( $E_R$ ), energy-to-moment ratio ( $E_R/M_0$ ), and apparent stress ( $\tau_\alpha$ ) for different rupture types at a global scale is examined by considering depth variations of mechanical properties, such as seismic velocities and rock densities, and rigidities. For this purpose, we used a 1-D global velocity model. The  $E_R/M_0$  ratio is, based on statistical  $t$ -tests, largest for strike-slip earthquakes, followed by normal-faulting events, with the lowest values for reverse earthquakes for hypocentral depths  $< 90$  km. Not enough data is available for statistical tests at deeper intervals except for the 90 to 120 km range, where we can satisfactorily conclude that  $E_R/M_0$  for R-SS and SS-R types is larger than for N type of faulting, which also conforms

29 to the previous assumption. In agreement with previous studies, our results exhibit a robust variation of  
30  $\tau_\alpha$  with the focal mechanism. Regarding the behavior of  $\tau_\alpha$  with depth, our results agree with the  
31 existence of a bimodal distribution with two depth intervals where the apparent stress is maximum for  
32 normal-faulting earthquakes. At depths in the range of 180 - 240 km,  $\tau_\alpha$  for reverse earthquakes is  
33 higher than for normal-faulting events. We find the trend  $E_U > E_{mt} > E_O$  for all mechanism types based  
34 on statistical  $t$ -tests. Finite-fault energy estimations also support focal mechanism dependence of  
35 apparent stress, but only for shallow earthquakes ( $Z < 30$  km). The slip distribution population used  
36 was too small to conclude that finite-fault energy estimations support the dependence of average  
37 apparent stress on rupture type at different depth intervals.

38

## 39 **1 Introduction**

40 The radiated seismic energy ( $E_R$ ) is a crucial source parameter that accounts for the size of an  
41 earthquake. The seismic energy is also a valuable parameter for understanding the dynamics of the  
42 rupture, especially in the case of large and complex earthquake sources (Venkataraman and Kanamori,  
43 2004a; Convers and Newman, 2011). The radiated seismic energy is considered the main contribution  
44 to the total seismic energy during the failure process (the sum of radiated energy, fracture energy, and  
45 thermal energy) (Boatwright and Choy, 1986). The most common approach to calculating  $E_R$  requires  
46 the integration of radiated energy flux in velocity-squared seismograms (Haskell, 1964; Thatcher and  
47 Hanks, 1973; Boatwright, 1980; Kanamori et al., 1993; Boatwright and Choy, 1986; Singh and Ordaz,  
48 1994; Choy and Boatwright, 1995; Pérez-Campos and Beroza, 2001). In order to recover the  $E_R$  of an  
49 event, the seismic records have to be corrected for propagation path and source effects such as  
50 attenuation, site effects, geometric spreading, radiation pattern, and directivity. Information on the  
51 Earth's structure is required to calculate seismic energy since  $E_R$  needs to be measured over a broad  
52 range of distances. Inaccurate information on the Earth's structure results in uncertainties in energy

53 estimations, particularly at higher frequencies (Venkataraman and Kanamori, 2004a). Furthermore,  
54 previous studies showed that estimates of  $E_R$  based on regional and teleseismic data might differ by as  
55 much as a factor of 10 for the same earthquake (Singh and Ordaz, 1994).

56

57 Choy and Boatwright (1995) reported a focal mechanism dependence of  $E_R$ . Later, this observation was  
58 confirmed by Pérez-Campos and Beroza (2001) but showed that the mechanism dependence is not as  
59 strong as reported previously. The degree of dependence of seismic energy on the focal mechanism is  
60 affected by several factors that bias the estimate (e.g., uncertainties in the corner frequency, geometrical  
61 spreading, hypocentral depth, and focal mechanism) (Pérez-Campos and Beroza, 2001). This  
62 dependence can be expressed in terms of the apparent stress ( $\tau_\alpha = \mu E_R/M_0$ , where  $\mu$  is the rigidity, Wyss  
63 and Brune, 1968), energy-to-moment ratio ( $E_R/M_0$ ), or slowness parameter ( $\Theta = \log_{10}(E_R/M_0)$ , Newman  
64 and Okal, 1998). Previous studies showed that strike-slip events have the highest apparent stress ( $\tau_\alpha =$   
65 0.70 MPa), followed by normal-faulting and thrust earthquakes with 0.25 and 0.15 MPa, respectively  
66 (Pérez-Campos and Beroza, 2001). On the other hand, some authors have observed that the  $E_R/M_0$  ratio  
67 is different for different types of earthquakes, particularly in subduction zones. For example, tsunami  
68 earthquakes have the smallest  $E_R/M_0$  ratio ( $7 \times 10^{-7} - 3 \times 10^{-6}$ ), interplate and downdip events have a  
69 slightly larger ratio ( $5 \times 10^{-6} - 2 \times 10^{-5}$ ), and intraplate and deep earthquakes have  $E_R/M_0$  ratios similar  
70 to crustal earthquakes ( $2 \times 10^{-5} - 3 \times 10^{-4}$ ) (Venkataraman and Kanamori, 2004a). The origin of the  
71 focal mechanism dependence is unclear, but it has been proposed that the stress drop is the cause of this  
72 dependence of the radiated seismic energy on the type of faulting (Pérez-Campos and Beroza, 2001).

73

74 Other approaches have also been used to calculate seismic energy, such as those based on finite-fault  
75 models (Ide, 2002; Venkataraman and Kanamori, 2004b; Senatorski, 2014). Ide (2002) calculated the  
76 radiated energy using an expression based on slip and stress on the fault plane. Energy estimates from

77 this method tend to be smaller by about a factor of 3 compared with the integrating far-field waveforms  
78 method. Venkataraman and Kanamori (2004b) used a formula for the energy radiated seismically from  
79 a finite source as a function of the time-dependent seismic moment  $M_0(t)$  and the properties of the  
80 medium. Here, the moment rate function derived from kinematic inversion is used to calculate the  $E_R$ .  
81 On the other hand, Senatorski (2014) used an overdamped dynamics approximation for estimating the  
82 radiated seismic energy. The accuracy of this method depends on the rupture history. This approach  
83 provides two energy parameters: 1) The finite-fault overdamped dynamics approximation ( $E_O$ ) and 2)  
84 the energy obtained from the averaged finite-fault model ( $E_U$ ). In both cases, the seismic energy  
85 depends on the slip, rupture time, and seismic moment. According to Senatorski (2014), in most cases,  
86 the radiated seismic energy estimated by integrating digital seismic waveforms ( $E_R$ ) is in the following  
87 range:  $E_U < E_R < E_O$ . Several seismic energy observations have been calculated and compiled in  
88 catalogs in the last two decades. In this study, we reexamine the possible dependence of seismic energy  
89 on the focal mechanism with an additional classification based on the type of rupture, considering pure  
90 and oblique mechanisms separately. We also investigate the potential influence of focal mechanisms on  
91 the derived estimates of radiated seismic energy from finite-fault models. Additionally, we explored the  
92 relationship between depth and the variables  $E_R/M_0$  and  $\tau_a$ . Furthermore, we established conversion  
93 relationships between various types of energy estimates. These findings play a crucial role in  
94 enhancing our understanding of the rupture processes associated with different types of earthquakes.

95

## 96 **2 Data and methods**

### 97 **2.1 Data**

98 We retrieved and classified focal mechanism solutions from the global centroid-moment-tensor catalog  
99 (gCMT) (Ekström et al., 2012) using a ternary diagram based on the Kaverina et al. (1996) projection.

100 This approximation classifies focal mechanism into seven classes of earthquakes: 1) normal (N); 2)



101 normal – strike-slip (N-SS); 3) strike-slip – normal (SS-N); 4) strike-slip (SS); 5) strike-slip – reverse  
102 (SS-R); 6) reverse – strike-slip (R-SS); and 7) reverse (R) (Fig. 1). For implementing fault-plane  
103 classification, we used the software FMC developed by Álvarez-Gómez (2019). Additionally, we used  
104 radiated seismic energy data and finite-fault models reported by the Incorporated Research Institutions  
105 for Seismology (IRIS) and the United States Geological Survey (USGS), respectively. To have  
106 homogeneity in the analyzed data, we do not include seismic energy observations and finite-fault  
107 models from other sources to avoid bias. IRIS reported automated  $E_R$  solutions for global earthquakes  
108 with an initial magnitude above  $M_w$  6.0. We studied 3331 events worldwide during the period April  
109 1990 – October 2022 (Fig. 2). Results include broadband energy solution (frequency band in the  
110 interval of 0.5 – 70 s) from vertical-component seismograms recorded at teleseismic distances ( $25^\circ \leq \Delta$   
111  $\leq 80^\circ$ ) (Convers and Newman, 2011; Hutko et al., 2017). Finite-fault models are determined with a  
112 kinematic inversion based on the wavelet domain (Ji et al., 2002). The procedure jointly inverts body  
113 and surface waves on a fault plane aligned with focal mechanism estimates from USGS W-phase or  
114 gCMT solutions. We used 231 finite-fault models from 1990 to 2022 (Fig. 2). After classifying the  
115 events, we determined scaling relationships for the reported seismic energies and analyzed the behavior  
116 of the  $E_R/M_0$  ratio and  $\tau_\alpha$ . The seismic energy was also determined using finite-fault models with the  
117 techniques described in the following section to know if there is a difference in estimates related to the  
118 faulting type. Seismic velocities and rock densities were taken from the ak135-F velocity model  
119 (Kennett et al., 1995; Montagner and Kennett, 1995); rigidity was calculated as  $\mu = \rho\beta^2$ .

120

## 121 **2.2 Methods**

### 122 **2.2.1 Radiated seismic energy derived from seismic waves**

123 In the following, we describe the procedure to calculate  $E_R$  implemented by IRIS and used as input to  
124 calculate apparent stress, energy-to-moment, and scaling relationships. Reported radiated seismic

125 energies from IRIS were calculated with the method of Boatwright and Choy (1986) implemented by  
 126 Convers and Newman (2011). Using velocity seismograms of the  $P$ -wave group (consisting of  
 127  $P+pP+sP$  phases), the energy is calculated at teleseismic distances. The seismic energy flux from the  $P$ -  
 128 wave group ( $\varepsilon_{gP}$ ) is calculated from the velocity spectrum ( $\dot{u}(\omega)$ ) as:

$$130 \quad \varepsilon_{gP} = \frac{\rho(z)\alpha(z)}{\pi} \int_0^{\infty} |\dot{u}(\omega)|^2 \exp(\omega t_{\alpha}^*) d\omega \quad , \quad (1)$$

131  
 132 where  $\rho(z)$  and  $\alpha(z)$  are the density and  $P$ -wave velocity at the source depth ( $z$ ), and the exponential  
 133 term  $t_{\alpha}^*$  corrects for anelastic attenuation. Subsequently, the energy flux is corrected for geometrical  
 134 spreading, radiation pattern, and partitioning between  $P$  and  $S$  waves. The radiated seismic energy at a  
 135 given station is calculated as:

$$137 \quad E_R^P = 4\pi \langle F^P \rangle^2 \left( \frac{R^P}{F^{gP}} \right)^2 \varepsilon_{gP} \quad , \quad (2)$$

138  
 139 where  $\langle F^P \rangle^2$  is the mean radiation pattern coefficient for  $P$ -waves,  $R^P$  is the geometrical spreading  
 140 factor of  $P$ -waves,  $F^{gP}$  is the generalized radiation pattern coefficient for the  $P$ -wave group.

$$142 \quad (F^{gP})^2 = (F^P)^2 + (PP F^{pP})^2 + \frac{2\alpha(z)}{3\beta(z)} q (CSP F^{sP})^2 \quad , \quad (3)$$

143  
 144 where  $\beta(z)$  is the  $S$ -wave velocity at the source depth,  $C$  is the correction for wavefront sphericity,  $F_p$ ,  
 145  $F_{pP}$ , and  $F_{sP}$  are radiation pattern coefficients for the  $P$ ,  $pP$ , and  $sP$  waves, respectively (Aki and

146 Richards, 1980). The parameter  $q$  represents the relative partitioning between  $S$  and  $P$  waves (using  $q =$   
 147 15.6, Boatwright and Fletcher, 1984).  $PP$  and  $SP$  are the reflection coefficients for the  $pP$  and  $sP$  wave  
 148 phases at the free surface. Finally, the radiated seismic energy obtained from the  $P$ -wave or  $S$ -wave  
 149 groups can be estimated with the formulae  $E_R = (1 + q)E_R^P = (1 + 1/q)E_R^S$ . For each event, the final  
 150 assigned seismic energy is the average for all the stations used.

151

## 152 2.2.2 Radiated energy estimations from finite-fault slip models

153 Senatorski (2014) introduced a method to estimate energy parameters derived from kinematic slip  
 154 models. In this method, the radiated seismic energy is expressed in terms of slip velocities using an  
 155 overdamped dynamics approximation (Senatorski, 1994; 1995). The method provides two energy  
 156 parameters: 1) the overdamped dynamics energy approximation ( $E_O$ ) and 2) the uniform model energy  
 157 estimation ( $E_U$ ). The accuracy of the overdamped dynamics solutions depends on the rupture history.  
 158 Senatorski (2014) showed that in most cases,  $E_U < E_R < E_O$ . The energy parameter  $E_O$  is calculated as:

159

$$160 \quad E_O = \frac{1}{2\beta(z)} \sum_i M_0^i V^i, \quad (4)$$

161

162 where  $\beta(z)$  is the shear wave velocity at the source depth and  $M_0^i$  is the seismic moment released at  
 163 the  $i$ -th fault segment.  $V^i$  is given by  $V^i = D^i/t_R^i$ , and  $D^i$ , and  $t_R^i$  are the slips and risetimes at the  $i$ -th  
 164 segment, respectively. The averaged finite-fault model estimation assumes uniform slip ( $\bar{D}$ ), and  
 165 slip velocity ( $V = \bar{D}/T$ ), so

166

$$167 \quad E_U = \frac{1}{2\beta(z)} M_0 V, \quad (5)$$

168

169 where  $M_0$  is the total seismic moment, and  $T$  is the rupture duration.

170

### 171 2.2.3 Radiated energy estimates based on moment rate functions of slip models

172 The radiated seismic energy can also be calculated through moment rate functions of finite-fault  
173 models (Haskell, 1964; Aki and Richards, 1980; Rudnicki and Freud, 1981; Venkataraman and  
174 Kanamori, 2004b). By ignoring the contribution from  $P$ -waves, which accounts for less than 5 % of the  
175 total radiated energy, the radiated energy derived from moment rate functions ( $E_{mrt}$ ) can be written as  
176 (Venkataraman and Kanamori, 2004b):

177

$$178 \quad E_{mrt} = \frac{1}{10 \pi \rho(z) \beta^5(z)} \int_0^{\infty} |\ddot{M}(t)_0|^2 dt \quad ,$$

179

180 where  $\rho(z)$  and  $\beta(z)$  are the density and  $S$ -wave velocity, respectively, at the source depth, and  $\ddot{M}(t)_0$   
181 is the derivative of the moment rate function (  $\dot{M}_0(t)$  ) estimated from a finite-fault model.

182

## 183 3 Results

184 We used different methods to quantify the radiated seismic energy. Table 1 shows the calculated scaling  
185 relationships for  $E_R$  for each energy method and type of faulting. Figs. 3, 4, 5, and 6 display the energy  
186 scaling relations derived from the velocity flux integration ( $E_R$ ), overdamped dynamics energy  
187 approximation ( $E_O$ ), the uniform model energy estimation ( $E_U$ ), and moment rate function methods  
188 ( $E_{mrt}$ ), respectively. Our results show some disparities in the calculated radiated seismic energies  
189 obtained with different techniques or data types. After carrying out rigorous statistical  $t$ -tests, when  
190 comparing  $E_R$  with the other methods to estimate seismic energy, we find that  $E_O$  estimates are always

191 lower than  $E_{\text{mrt}}$  and  $E_U$ , while  $E_U$ 's estimates are the highest (Tables S1 to S3). The lowest average  
192 difference factors are for  $E_O$  estimates, ranging from 0.28 to 0.77 (Fig. 7). Conversely, mean difference  
193 factors can be as high as 20 for  $E_U$  estimations (Fig. 8). Average difference factors exhibit intermediate  
194 values for  $E_{\text{mrt}}$  calculations, fluctuating from 1.53 to 3.27 (Fig. 9). These relations stand regardless of  
195 the rupture type (Tables S1 to S3, and Figs. 7 to 9). Conversion relationships between  $E_R$  and  $E_O$ ,  $E_U$ ,  
196 and  $E_{\text{mrt}}$  are presented in Table 2, which may be helpful when considering either estimation method.

197

198 In terms of the  $E_R/M_0$  ratio, our results show that SS, SS-N, and SS-R events have the highest mean  
199 values ( $3.06 \times 10^{-5} < E_R/M_0 < 3.75 \times 10^{-5}$ ) (Fig. 10). R-SS earthquakes have a slightly lower mean ratio  
200 ( $E_R/M_0 = 2.87 \times 10^{-5}$ ) (Fig. 10). Average  $E_R/M_0$  ratio fluctuates from  $2.31 \times 10^{-5}$  to  $2.37 \times 10^{-5}$  for N-SS  
201 and N events, respectively (Fig. 10). On the other hand, the lowest values of  $E_R/M_0$  are related to R  
202 earthquakes ( $E_R/M_0 = 1.70 \times 10^{-5}$ ) (Fig. 10). Statistical tests confirm this trend since we find that, in  
203 general, and for data where there is a significant difference: SS, N-SS, R-SS, SS-N, SS-R > N > R  
204 (Tables S4 to S10). The same trend is repeated for events in the  $Z < 30$  km,  $30 < Z < 60$  km, and  $60 < Z$   
205  $< 90$  km depth ranges. For the  $90 < Z < 120$  km depth range, we can only confidently state that RSS >  
206 N and SSR > N due to a lack of data. Most of the rupture types present a differentiated behavior of  
207  $E_R/M_0$  in terms of depth with the existence of two clusters, above and below about 300 km depth (Fig.  
208 11). In contrast, strike-slip earthquakes demonstrate a distinct pattern, with the majority of  $E_R/M_0$   
209 observations concentrated at depths shallower than 50 km (Fig. 11). Furthermore, at shallow depths, the  
210 radiated energy-to-moment ratio shows large variability compared to observations of deep earthquakes  
211 (Fig. 11).

212

213 Previous studies have provided evidence that mean apparent stress estimates can be obtained using  
214 regression models, specifically through the equation  $\log_{10} E_R = \log_{10} M_0 + b$  with  $\tau_\alpha = \mu 10^b$ , supporting

215 the focal mechanism dependence of  $E_R$  (Choy and Boatwright, 1995; Pérez-Campos and Beroza, 2001).  
216 To test that this dependence persists with depth, we conducted regressions every 30 km of depth  
217 considering variations of  $\mu$  and at least ten observations. First, we evaluated reported seismic energy  
218 observations based on the velocity flux integration method (Table 3). Considering the distinct statistical  
219 differences in the  $E_R/M_0$  ratios across various rupture types, it can be justified that the  $\tau_\alpha$  results exhibit  
220 a similar pattern, as they are derived through multiplication with a consistent scaling factor determined  
221 by the value of  $\mu$ . Thus, our results agree with previous studies where  $\tau_\alpha$  follows the following behavior  
222 (R-SS, R) < (N-SS, N) < (SS, SS-N, SS-R) in the range of 0 – 180 km (Table 3). Conversely,  $\tau_\alpha$  is  
223 higher for R events than for N earthquakes at depths from 180 to 240 km (Table 3). At depths higher  
224 than 240 km, only N events were obtained under the assumptions considered. In Table 3, we  
225 summarized results for all the depth intervals showing the mean values and their 95% log-normal  
226 geometric spread.

227

228 Our results also showed that N and N-SS events exhibit a bimodal distribution of  $\tau_\alpha$  with depth (Fig.  
229 12). The most significant values of  $\tau_\alpha$  occur in two depth ranges of approximately 40 – 60 km and 580 –  
230 650 km, where maximum apparent stresses approach 8 and 16 MPa, respectively (Fig. 12). N-SS, R, R-  
231 SS, SS-N, and SS-R events also showed two maximum values of  $\tau_\alpha$  ranging from 7 to 11 MPa and 9 to  
232 15 MPa for shallow and deep earthquakes, respectively (Fig. 12). For SS events, there is only one depth  
233 range over which  $\tau_\alpha$  shows maxima. In this case, the highest values of  $\tau_\alpha$  are found in the higher depth  
234 range from 50 to 100 km ( $\tau_\alpha \sim 12$  MPa) (Fig. 12). On the other hand, the average apparent stress  
235 estimates based on the finite-fault models exhibit a similar dependence on the focal mechanism than  
236 those obtained with the velocity flux integration method at shallow depths ( $Z < 30$  km) (Table 4).  
237 Regressions showed that  $\tau_\alpha$  follows the following behavior R < N < (SS, SS-R) for  $E_U$  and  $E_{mt}$   
238 estimations (Table 4). In contrast,  $E_O$  showed no clear dependence of  $\tau_\alpha$  with the focal mechanism

239 (Table 4). Due to the constraint of at least ten observations (slip distributions) for each 30 km depth  
240 interval, we could not analyze the dependence of  $\tau_\alpha$  on the type of faulting at a deeper depth.

241

#### 242 **4 Discussion**

243 In this study, we analyzed radiated seismic energy and parameters that measure the amount of energy  
244 per unit of the moment, such as the apparent stress and the energy-to-moment ratio (also known as  
245 scaled energy or apparent strain), considering their respective particularities. The advantage of using  $\tau_\alpha$   
246 is that it can be related to other stress processes associated with the seismic rupture, such as the stress  
247 drop. On the other hand, many finite-fault models of the spatiotemporal slip history for moderate and  
248 large earthquakes exist. From these models, important information can be extracted, such as fault  
249 dimensions (Mai and Beroza, 2000), static stress drop (Ripperger and Mai, 2004), or radiated seismic  
250 energy (Ide, 2002; Senatorski, 2014). When using finite-fault models to determine  $E_R$ , it is necessary to  
251 consider that they usually explain low-frequency seismic waves. However, the higher-frequency wave  
252 contribution is necessary for calculating the total radiated seismic energy. This issue brings differences  
253 among finite-fault energy estimates and those from integrating far-field waveforms.

254

255 Furthermore, finite-fault seismic energy estimations are strongly affected by event location, the number  
256 of available data, faulting parameterization, and velocity structure. The degree of discrepancy between  
257 the finite-fault energy estimates ( $E_{mt}$ ,  $E_O$ , and  $E_U$ ) with respect to the velocity flux integration method  
258 ( $E_R$ ) is variable among the different types of seismic energy. For example, the moment rate functions  
259 are relatively robustly determined by teleseismic data, while rupture dimensions are strongly affected  
260 by model parameters (Ye et al., 2016). This may explain why the average difference factor ( $E_R/E_U$ ) is  
261 greater than the  $E_R/E_{mt}$  factor (Figs. 8 and 9). Another source of discrepancies in finite-fault energy  
262 calculations comes from the spatial and temporal smoothing in resolving the kinematic slip distribution

263 and the rupture velocity assigned. Errors associated with the assumptions are tough to quantify as they  
264 propagate into the energy estimates in complex ways.

265

266 Our results agree with previous estimates of  $E_O$  and  $E_U$ , confirming that  $E_R$  is in the range of  $E_U - E_O$  for  
267 most earthquakes. The overdamping approximation ( $E_O$ ) can be used to characterize the heterogeneity  
268 of the rupture process. Senatorski (2014) states that if the ratio  $E_O/E_R$  is  $< 0.4$ , the rupture can be  
269 represented as a simple dislocation rupture.  $E_O/E_R > 1$  is expected in the case of heterogeneous rupture  
270 processes. On the other hand, some of the suggested explanations for the observation that  $E_O > E_R$  are:  
271 1) the finite-fault slip models require refinement; 2) the seismic energy estimations require correction  
272 for directivity, modified attenuation factors, or sites effects; and 3) some other factors are not  
273 considered in the calculations such as the fact that the energy dissipation is not taken into account by  
274 the planar faults (Senatorski, 2014).

275

276 The radiated seismic energy scaled by seismic moment is an essential characterization of earthquake  
277 dynamics. The low  $E_R/M_0$  of reverse events is associated with tsunami earthquakes being compatible  
278 with the results of previous studies (Newman and Okal, 1998; Venkataraman and Kanamori, 2004a;  
279 Convers and Newman, 2011; Ye et al., 2016). Our results showed that  $E_R/M_0$  has a large scatter from  $6$   
280  $\times 10^{-7}$  to  $2 \times 10^{-4}$  for all the rupture types. However, no evident magnitude dependence can be asserted  
281 (Fig. 10). One of the reasons for the dispersion of  $E_R/M_0$  is that it depends on many seismogenic  
282 properties of the source region (Fig. 10). As a consequence,  $E_R/M_0$  varies significantly in different  
283 tectonic environments and deep conditions such as pressure and temperature (Fig. 11). Even within the  
284 same tectonic environment,  $E_R/M_0$  has significant variations, as has been reported by Plata-Martínez et  
285 al. (2019) in the Middle American Trench, where variations in  $E_R/M_0$  are associated with  
286 heterogeneities along the trench, such as asperities. The different types of earthquakes have differences



287 in the frequency content of the seismic energy released.

288

289 Venkataraman and Kanamori (2004a) reported that  $E_R/M_0$  is in the range of  $5 \times 10^{-6} - 2 \times 10^{-5}$  for  
290 interplate and downdip earthquakes, which are mainly consistent with reverse and normal faulting. Our  
291 results show that the average values of  $E_R/M_0$  for R and N events are  $1.70 \times 10^{-5}$  and  $2.37 \times 10^{-5}$ ,  
292 respectively, and both values are within the interval defined by Venkataraman and Kanamori (2004a).

293 The  $E_R/M_0$  ratio for deep earthquakes varies from  $2.0 \times 10^{-5}$  to  $3.0 \times 10^{-4}$  (Venkataraman and Kanamori,  
294 2004a). We found that  $E_R/M_0$  for deep earthquakes of all types of rupture is in the interval of  $2 \times 10^{-6} -$   
295  $2 \times 10^{-4}$  but with a predominance of  $1.0 \times 10^{-5} > E_R/M_0$  (Fig. 11). Despite the  $E_R/M_0$  scatter, our results  
296 depict a general trend for the average values of  $E_R/M_0$ , which can be expressed as  $R < (N, N\text{-SS}, R\text{-SS})$   
297  $< (SS, SS\text{-R}, SS\text{-N})$  (Fig. 10), a similar tendency was reported by Convers and Newman (2011) where  
298  $E_R/M_0$  follows  $R < N < SS$ .

299

300 Our results support  $E_R$ 's previously reported focal mechanism dependence (Choy and Boatwright, 1995;  
301 Pérez-Campos and Beroza, 2001; Convers and Newman, 2011) but narrow the range. Examination of  
302 mean  $\tau_\alpha$  with various focal mechanisms and at different depths has been done for different earthquake  
303 sizes and tectonic settings. We identified the largest values of apparent stress for strike-slip events,  
304 intermediate values for normal-faulting events, and lowest for reverse-faulting events in the depth  
305 interval of 0 – 180 km (Table 3). On the other hand, our results showed that at depths between 180 and  
306 240 km,  $\tau_\alpha$  for reverse earthquakes is higher than for normal-faulting events. This can be explained; for  
307 example, deep reverse earthquakes in subduction zones occur in the slab's lower part, where they are  
308 subjected to significantly large compressive stresses. A precise characterization of the depth  
309 dependence of  $\tau_\alpha$  remains unclear at depths greater than 240 km. In Table 3, we present and compare  
310 our results for  $\tau_\alpha$ , supporting the observation of the dependence of  $E_R$  on the type of faulting. The origin

311 of this focal dependence is unclear, but it has been raised that it reflects a mechanism-dependent  
312 difference in stress drop (Pérez-Campos and Beroza, 2001). It can be highlighted with an alternative  
313 definition for the apparent stress, assuming that the dynamic and static stress drops are roughly  
314 equivalent. Then  $\tau_\alpha$  can be expressed as  $\tau_\alpha = (\eta_R \Delta\sigma)/2$ , where  $\eta_R$  is the seismic efficiency, and  $\Delta\sigma$  is the  
315 stress drop (Convers and Newman, 2011). Allmann and Shearer (2009) provided additional information  
316 to support the role of stress drop on the dependency of apparent stress with the type of faulting. They  
317 found a dependence of median stress drop on the focal mechanism with a factor of 3–5 times higher  
318 stress drops for strike-slip events and two times higher stress drops for intraplate events compared to  
319 interplate events.

320

321 Nevertheless, other interpretations of the apparent stress variation are related to the mechanical  
322 properties of the rock, such as the reduction of rigidity in shallow subduction environments or  
323 increment in lithostatic pressure if no change in regional rigidity is assumed (Convers and Newman,  
324 2011). The variation of such estimates concerning expected spatial variations in rigidity is an issue that  
325 still needs attention. Choy and Kirby (2004) also suggested that  $\tau_\alpha$  can be related to fault maturity. For  
326 example, lower stress drops are needed to reach rupture in mature faults. On the contrary, earthquakes  
327 generated at immature faults (low cumulative displacement) radiate more energy per unit of seismic  
328 moment. Regarding the behavior of  $\tau_\alpha$  with depth, our results agree with the existence of a bimodal  
329 distribution with two depth intervals where the apparent stress is maximum for normal-faulting  
330 earthquakes, as reported by Choy and Kirby (2004). We also found that almost all types of faulting (SS-  
331 N, SS-R, R-SS, R, N-SS, and N) show two depth ranges where the stress is maximum, but in the case  
332 of normal-faulting earthquakes, it is very well defined. On the other hand, almost all strike-slip  
333 earthquakes show a single interval of depths where the apparent stress is maximum (Fig. 12).  
334 Earthquakes with an oblique focal mechanism show a mixed behavior of  $\tau_\alpha$ , as is the case of the SS-N

335 and SS-R events that present similar characteristics to normal and reverse earthquakes in terms of the  
336 depth distribution of  $\tau_\alpha$ .

337

338 In terms of the spatial distribution of  $E_R$  and  $\tau_\alpha$  (Figs. S1 to S14), the highest values of  $\tau_\alpha$  for N events  
339 are located at the border between the Nazca and South American plates, the Eurasian and Philippine  
340 plates, the Indo-Australian and Pacific plates, the Philippine and Pacific plates, and the Pacific and  
341 North American plates (in the Alaska region) (Fig. S1). Regarding the seismic energy of earthquakes,  
342 the regions where the most energetic earthquakes have occurred concur with the aforementioned areas,  
343 with the addition of the border between the Cocos and North American plates (Fig. S2). The high  $\tau_\alpha$   
344 normal-faulting events are associated with regions of intense deformation, such as a sharp slab bending  
345 or zones where opposing slabs collide (Choy and Kirby, 2004). At shallow depths ( $Z < 35$  km), high- $\tau_\alpha$   
346 events are related to the beginning of the subduction beneath the overriding plate (Choy and Kirby,  
347 2004). Our results support the observation that the average apparent stress of intraslab normal-faulting  
348 events is considerably higher than the average  $\tau_\alpha$  of interplate thrust-faulting earthquakes reported by  
349 Choy and Kirby (2004) (Figs. S1 and S5).

350

351 In the case of R earthquakes, the highest values of  $E_R$  and  $\tau_\alpha$  are in the limit of the Eurasian and  
352 Philippine plates, the Nazca and South American plates, the Philippine and Pacific plates, the Indo-  
353 Australian and Pacific plates, and the Eurasian and Indo-Australian plates (Figs. S5 and S6). In  
354 contrast, strike-slip events with the highest values of  $E_R$  and  $\tau_\alpha$  are on the border between the African  
355 and Eurasian plates (in Türkiye), the Eurasian and Indo-Australian plates, the Philippine and Eurasian  
356 plates, the Indo-Australian and Pacific plates (in New Zealand), and the Caribbean and South American  
357 plates (Figs. S13 and S14). We have found that several SS earthquakes are located in the oceanic  
358 lithosphere at depths  $< 50$  km. Many of the SS events with high  $\tau_\alpha$  are located near the plate-boundary

359 triple junctions where there are high rates of intraplate deformation, as previously reported by Choy  
360 and McGarr (2002).

361

362 Finally, when using seismic energy estimates based on finite-fault models ( $E_O$  and  $E_{mrt}$ ), a clear  
363 dependence of the average apparent stress with the focal mechanism is observed at shallow depths ( $Z <$   
364 30 km) (Table 4). For example, using  $E_U$  and  $E_{mrt}$ , the average  $\tau_\alpha$  follows  $R < N < (SS-R, SS)$ . If  $E_O$  is  
365 used, the mean apparent stress exhibits similar values for SS-R, N, and R events (Table 4). However,  
366 the lack of a significant number of observations for some types of earthquakes makes it challenging to  
367 evaluate the use of finite-fault models to determine apparent stress. Despite these limitations, the  
368 methods used to estimate the seismic energy based on finite-fault models are a quick alternative to  
369 calculate a range of energy variation once a slip distribution is obtained. Determining earthquake  
370 occurrence rates from the accumulated seismic moment is an established tool of seismic hazard  
371 analysis. The size of an earthquake can also be defined in terms of the radiated seismic energy.  
372 Incorporating the spatial distribution of seismic energy in seismic hazard analyses has the advantage  
373 that seismic energy is a better predictor of the damage potential of seismic waves than the seismic  
374 moment release. In that sense, our results can be used to improve global seismic hazard models.

375

## 376 **5 Conclusion**

377 We studied the radiated seismic energy, energy-to-moment ratio, and apparent stress for different types  
378 of faulting. Our data relies on different methodologies employing the velocity flux integration and  
379 finite-fault models to determine the seismic energy. The approach based on slip distributions involved  
380 the utilization of two techniques: 1) total moment rate functions and 2) overdamped dynamics  
381 approximation. We analyzed 3331 energy observations derived from integrating far-field waveforms.  
382 On the other hand, we used 231 finite-fault models. For all mechanism types,  $E_U > E_{mrt} > E_O$ , based on

383 statistical t-tests. Finite-fault energy estimations also support focal mechanism dependence of apparent  
384 stress, but only for shallow earthquakes ( $Z < 30$  km). The population of slip distributions used was too  
385 small to conclude that finite-fault energy estimations support the dependence of average apparent stress  
386 on rupture type at different depth intervals. The estimated energy differences are within the margin  
387 reported in the literature, which can reach a factor higher than 10. The methods used to estimate  
388 seismic energy based on finite fault models are an easily implemented alternative that gives results  
389 compatible with the seismic record integration technique, given the larger uncertainties of these  
390 methods. We also derived scaling relationships for the different types of energies and conversion  
391 relations.

392

393 In terms of the behavior of the  $E_R/M_0$  ratio, our results showed a high scatter without a clear  
394 dependence on magnitude. The  $E_R/M_0$  ratio is, based on statistical  $t$ -tests, the largest for strike-slip  
395 earthquakes, followed by normal-faulting events, with the lowest values for reverse earthquakes for  
396 hypocentral depths  $< 90$  km. Not enough data is available for statistical tests at deeper intervals except  
397 for the range 90 to 120 km, where we can satisfactorily conclude that  $E_R/M_0$  for R-SS and SS-R types is  
398 larger than for N type of faulting, which also conforms to the previous assumption. Regarding the  
399 behavior of  $\tau_\alpha$  with depth, our results agree with the existence of a bimodal distribution with two depth  
400 intervals where the apparent stress is maximum for normal-faulting earthquakes. At depths in the range  
401 of 180 - 240 km,  $\tau_\alpha$  for reverse earthquakes is higher than for normal-faulting events. Our  $E_R/M_0$   
402 estimates for deep earthquakes are also consistent with reported values. By analyzing the average  
403 apparent stress, our results also support the previously reported focal mechanism dependence of  $E_R$  at  
404 depths ranging from 0 to 180 km. We found that normal-faulting events have intermediate values of  $\tau_\alpha$   
405 between strike-slip and reverse events using the energy flux integration approach in agreement with  
406 previous studies.

407 On the other hand,  $\tau_\alpha$  for reverse earthquakes is higher than for normal-faulting events at depths  
408 between 180 and 240 km. In contrast, a clear focal mechanism dependence is observed when finite-  
409 fault methods are used to estimate the mean apparent stress at shallow depths ( $Z < 30$  km). This study's  
410 population of slip distributions was too small to conclude that finite-fault energy estimations support  
411 the mechanism dependence of average apparent stress at different depths. There are two depth ranges  
412 over which apparent stress for SS-N, SS-R, R-SS, R, N-SS, and N earthquakes shows maxima.

413 Earthquakes with an oblique focal mechanism show a mixed behavior of energy parameters since it has  
414 common characteristics of two types of faults; in some cases, one of them predominates over the other.  
415  
416 Code availability. Generic Mapping Tools (GMT5) is available at <http://gmt.soest.hawaii.edu/>, last  
417 access: 19 June 2023. FMC is available at <https://github.com/Jose-Alvarez/FMC>, last access: 19 June  
418 2023.

419  
420 Data availability. Radiated seismic energy data are acquired from the IRIS Data Services Products:  
421 EQEnergy (<https://ds.iris.edu/ds/products/eqenergy/>). Focal mechanisms are taken from Global CMT  
422 catalog (<https://www.globalcmt.org/>). Finite-fault models are acquired from the USGS earthquake  
423 catalog (<https://earthquake.usgs.gov/earthquakes/search/>).

424  
425 Author contributions. QRP designed the idea, developed the methodology and performed the  
426 preliminary analyses. QRP and FRZ discussed and analyzed the results and wrote the paper.

427  
428 Competing interests. The authors declare that they have no conflict of interest.

429  
430 Acknowledgments. Quetzalcoatl Rodríguez-Pérez was supported by the Mexican National Council for

431 Humanities, Science, and Technology (CONAHCYT) (Cátedras program - project 1126).

432

433 Financial support. This research has been supported by the CONAHCYT (grant no. Catedras program,  
434 project 1126).

435

#### 436 **References**

437 Aki, K., Richards, P.G.: Quantitative seismology, 913 pp., W. H. Freeman, New York, 1980.

438

439 Allmann, B., Shearer, P.M.: Global variations of stress drop for moderate to large earthquakes, *J.*  
440 *Geophys. Res.*, 114, B01310, <https://doi.org/10.1029/2008JB005821>, 2009.

441

442 Álvarez-Gómez, J.A.: FMC-Earth focal mechanisms data management, cluster and classification,  
443 *Software X* 9, 299-307, <https://doi.org/10.1016/j.softx.2019.03.008>, 2019.

444

445 Boatwright, J.L.: A spectral theory for circular seismic sources; simple estimates of source dimension,  
446 dynamic stress drop, and radiated seismic energy, *Bull. Seism. Soc. Am.*, 70, 1-27,  
447 <https://doi.org/10.1785/BSSA0700010001>, 1980.

448

449 Boatwright, J.L., Fletcher, J.B.: The partition of radiated energy between *P* and *S* waves, *Bull. Seism.*  
450 *Soc. Am.*, 74, 361-376, <https://doi.org/10.1785/BSSA0740020361>, 1984.

451

452 Boatwright, J.L., Choy, G.L.: Teleseismic estimates of the energy radiated by shallow earthquakes, *J.*  
453 *Geophys. Res.*, 91, 2095-2112, <https://doi.org/10.1029/JB091iB02p02095>, 1986.

454

455 Choy, G.L., Boatwright, J.L.: Global patterns of radiated seismic energy and apparent stress, J.  
456 Geophys. Res 100, B9, 18205-18228, <https://doi.org/10.1029/95JB01969>, 1995.  
457

458 Choy, G.L., McGarr, A.: Strike-slip earthquakes in the oceanic lithosphere: observations of  
459 exceptionally high apparent stress, Geophys. J. Int., 150, 506-523, <https://doi.org/10.1046/j.1365->  
460 246X.2002.01720.x, 2002.  
461

462 Choy, G.L., Kirby, S.H.: Apparent stress, fault maturity and seismic hazard for normal-fault  
463 earthquakes at subduction zones, Geophys. J. Int., 159, 991-1012, <https://doi.org/10.1111/j.1365->  
464 246X.2004.02449.x, 2004.  
465

466 Convers, J.A., Newman, A.V.: Global evaluation of large earthquake energy from 1997 through mid-  
467 2010, J. Geophys. Res., 116, B08304, <https://doi.org/10.1029/2010JB007928>, 2011.  
468

469 Ekström, G., Nettles, M., Dziewoński, A.M.: The global CMT project 2004–2010: Centroid-moment  
470 tensors for 13,017 earthquakes, Phys. Earth Planet. Inter., 201-201, 1-9,  
471 <https://doi.org/10.1016/j.pepi.2012.04.002>, 2012.  
472

473 Haskell, N.A.: Total energy and energy spectral density of elastic wave radiation from propagating  
474 faults, Bull. Seism. Soc. Am., 54, 1811-1841, <https://doi.org/10.1785/BSSA05406A1811>, 1964.  
475

476 Hutko, A.R., Bahavar, M., Trabant, C., Weekly, R.T., Van Fossen, M., Ahern, T.: Data Products at the  
477 IRIS-DMC: Growth and Usage, Seismol. Res. Lett., 88, 892-903, <https://doi.org/10.1785/0220160190>,  
478 2017.



479

480 Ide, S.: Estimation of radiated energy of finite-source earthquake modes, *Bull. Seism. Soc. Am.*, 92,  
481 2994-3005, <https://doi.org/10.1785/0120020028>, 2002.

482

483 Ji, C., Wald, D.J., Helmberger, D.V.: Source description of the 1999 Hector Mine, California  
484 earthquake; Part I: Wavelet domain inversion theory and resolution analysis, *Bull. Seism. Soc. Am.*, 92,  
485 1192-1207, <https://doi.org/10.1785/0120000916>, 2002.

486

487 Kanamori, H., Mori, J., Hauksson, E., Heaton, T.H., Hutton, L.K., Jones, L.M.: Determination of  
488 earthquake energy release and  $M_L$  using terrascope, *Bull. Seismol. Soc. Am.*, 83, 330-346,  
489 <https://doi.org/10.1785/BSSA0830020330>, 1993.

490

491 Kaverina, A.N., Lander, A.V., Prozorov, A.G.: Global creepex distribution and its relation to  
492 earthquake-source geometry and tectonic origin, *Geophys. J. Int.*, 125, 249-265,  
493 <https://doi.org/10.1111/j.1365-246X.1996.tb06549.x>, 1996.

494

495 Kennett, B.L.N., Engdahl, E.R., Buland, R.: Constraints on seismic velocities in the earth from travel  
496 times, *Geophys. J. Int.*, 122, 108-124, <https://doi.org/10.1111/j.1365-246X.1995.tb03540.x>, 1995.

497

498 Mai, P.M., Beroza, G.C.: Source scaling properties from finite-fault-rupture models, *Bull. Seismol.*  
499 *Soc. Am.*, 90, 604-615, <https://doi.org/10.1785/0119990126>, 2000.

500

501 Montagner, J.P., Kennett, B.L.N.: How to reconcile body-wave and normal-mode reference Earth  
502 models?", *Geophys. J. Int.*, 125, 229-248, <https://doi.org/10.1111/j.1365-246X.1996.tb06548.x>, 1995.

503

504 Newman, A.V., Okal, E.A.: Teleseismic estimates of radiated seismic energy: the  $E/M_0$  discriminant for  
505 tsunami earthquakes, *J. Geophys. Res.*, 103, 26885-26898, <https://doi.org/10.1029/98JB02236>, 1998.

506

507 Pérez-Campos, X., Beroza, G.C.: An apparent mechanism dependence of radiated seismic energy, *J.*  
508 *Geophys. Res.*, 106, B6, 11127-11136, <https://doi.org/10.1029/2000JB900455>, 2001.

509

510 Plata-Martínez, R., Pérez-Campos, X., Singh, S.K.: Spatial distribution of radiated seismic energy of  
511 three aftershocks sequences at Guerrero, Mexico, subduction zone, *Bull. Seismol. Soc. Am.*, 109, 2556-  
512 2566, <https://doi.org/10.1785/0120190104>, 2019.

513

514 Ripperger, J., Mai, P.M.: Fast computation of static stress changes on 2D faults from final slip  
515 distributions, *Geophys. Res. Lett.*, 31, L18610, <https://doi.org/10.1029/2004GL020594>, 2004.

516

517 Rudnicki, J.W., Freund, L.B.: On energy radiation from seismic sources, *Bull. Seismol. Soc. Am.*, 71,  
518 583-595, <https://doi.org/10.1785/BSSA0710030583>, 1981.

519

520 Senatorski, P.: Spatio-temporal evolution of faults: deterministic model, *Physica D*, 76, 420-435,  
521 [https://doi.org/10.1016/0167-2789\(94\)90049-3](https://doi.org/10.1016/0167-2789(94)90049-3), 1994.

522

523 Senatorski, P.: Dynamics of a zone of four parallel faults: a deterministic model, *J. Geophys. Res.*, 100,  
524 B12, 24111-24120, <https://doi.org/10.1029/95JB02624>, 1995.

525

526 Senatorski, P.: Radiated energy estimations from finite-fault earthquake slip models, *Geophys. Res.*

527 Lett., 41, 3431-3437, <https://doi.org/10.1002/2014GL060013>, 2014.

528

529 Singh, S.K., Ordaz, M.: Seismic energy release in Mexican subduction zone earthquakes, Bull.

530 Seismol. Soc. Am., 84, 1533-1550, <https://doi.org/10.1785/BSSA0840051533>, 1994.

531

532 Thatcher, W., Hanks, T.C.: Source parameters of southern California earthquakes, J. Geophys. Res., 78,

533 8547-8576, <https://doi.org/10.1029/JB078i035p08547>, 1973.

534

535 Venkataraman, A., Kanamori, H.: Observational constraints on the fracture energy of subduction zone

536 earthquakes, J. Geophys. Res., 109, B05302, <https://doi.org/10.1029/2003JB002549>, 2004a.

537

538 Venkataraman, A., Kanamori, H.: Effect of directivity on estimates of radiated seismic energy, J.

539 Geophys. Res., 109, B04301, doi:10.1029/2003JB002548, <https://doi.org/10.1029/2003JB002548>,

540 2004b.

541

542 Wyss, M., Brune, J.N.: Seismic moment, stress, and source dimensions for earthquakes in the

543 California-Nevada region, J. Geophys. Res., 73, 4681-4694, <https://doi.org/10.1029/JB073i014p04681>,

544 1968.

545

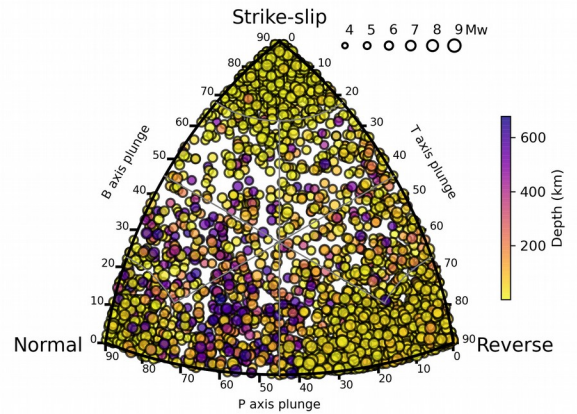
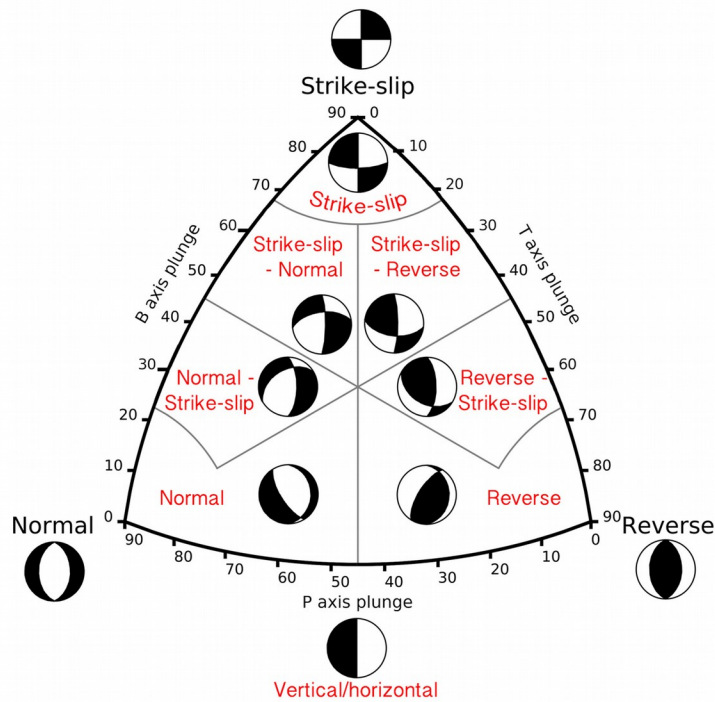
546 Ye, L., Lay, T., Kanamori, H., Rivera, L.: Rupture characteristics of major and great ( $M_w \geq 7.0$ )

547 megathrust earthquakes from 1990 to 2015: 1. Source parameter scaling relationships, J. Geophys.

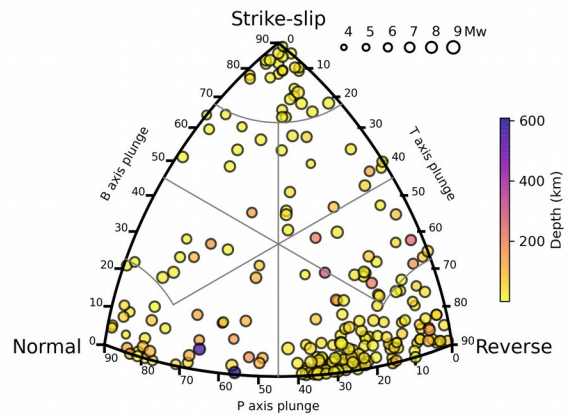
548 Res., 121, 826-844, <https://doi.org/10.1002/2015JB012426>, 2016.

549

550



Er observations



Finite-fault

551

552

553 **Figure 1.** The Kaverina fault classification ternary diagram used to classify focal mechanisms (left  
 554 panel). Focal mechanisms are denoted by circles filled to indicate event depth in km, and the size of the  
 555 circle indicates the moment magnitude of the earthquake (right panels). The upper right panel shows  
 556 the rupture type of seismic events with a radiated seismic energy estimation. Rupture type of seismic  
 557 events with a finite-fault model used to estimate the radiated energy (lower right panel).

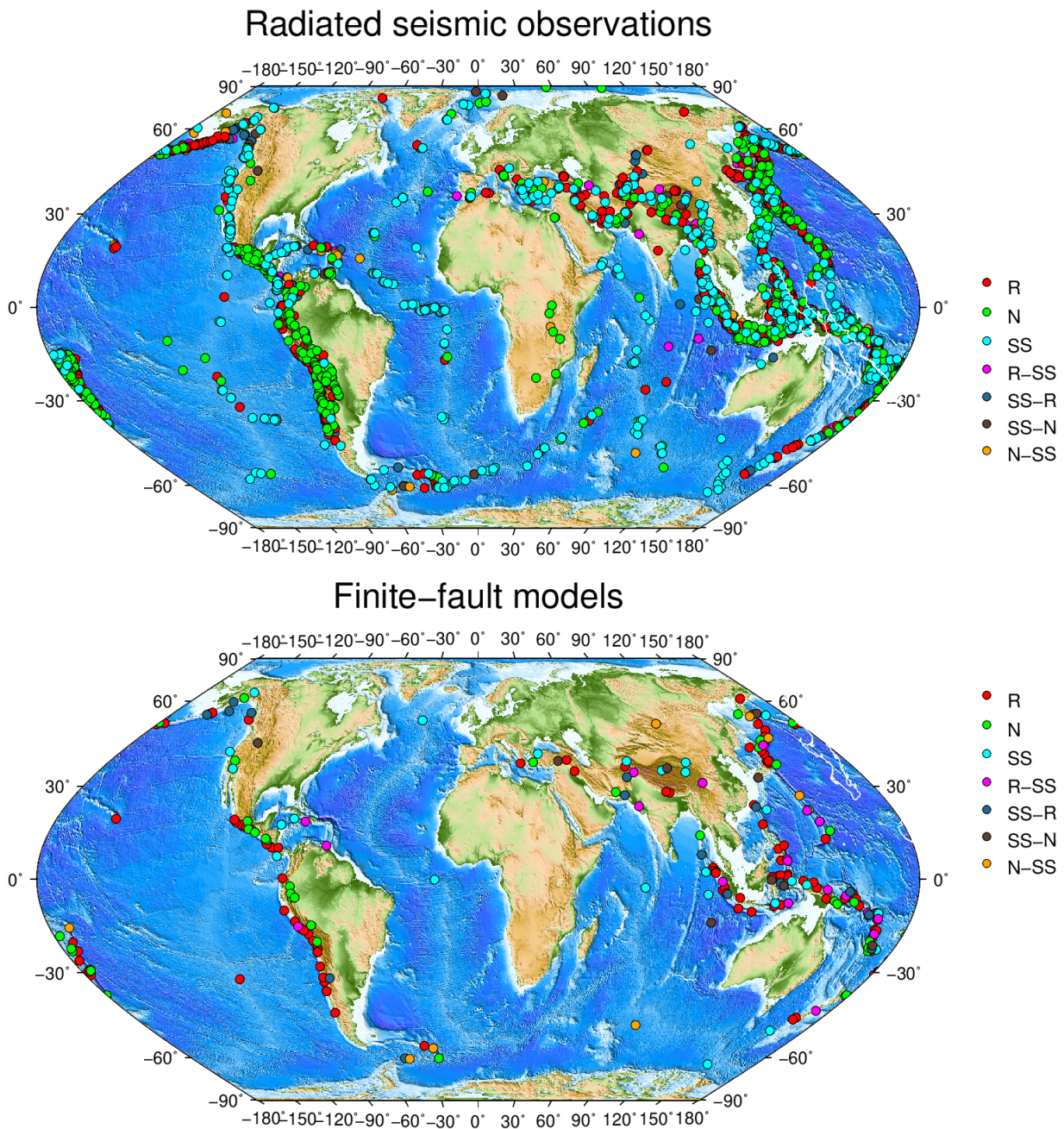
558

559

560

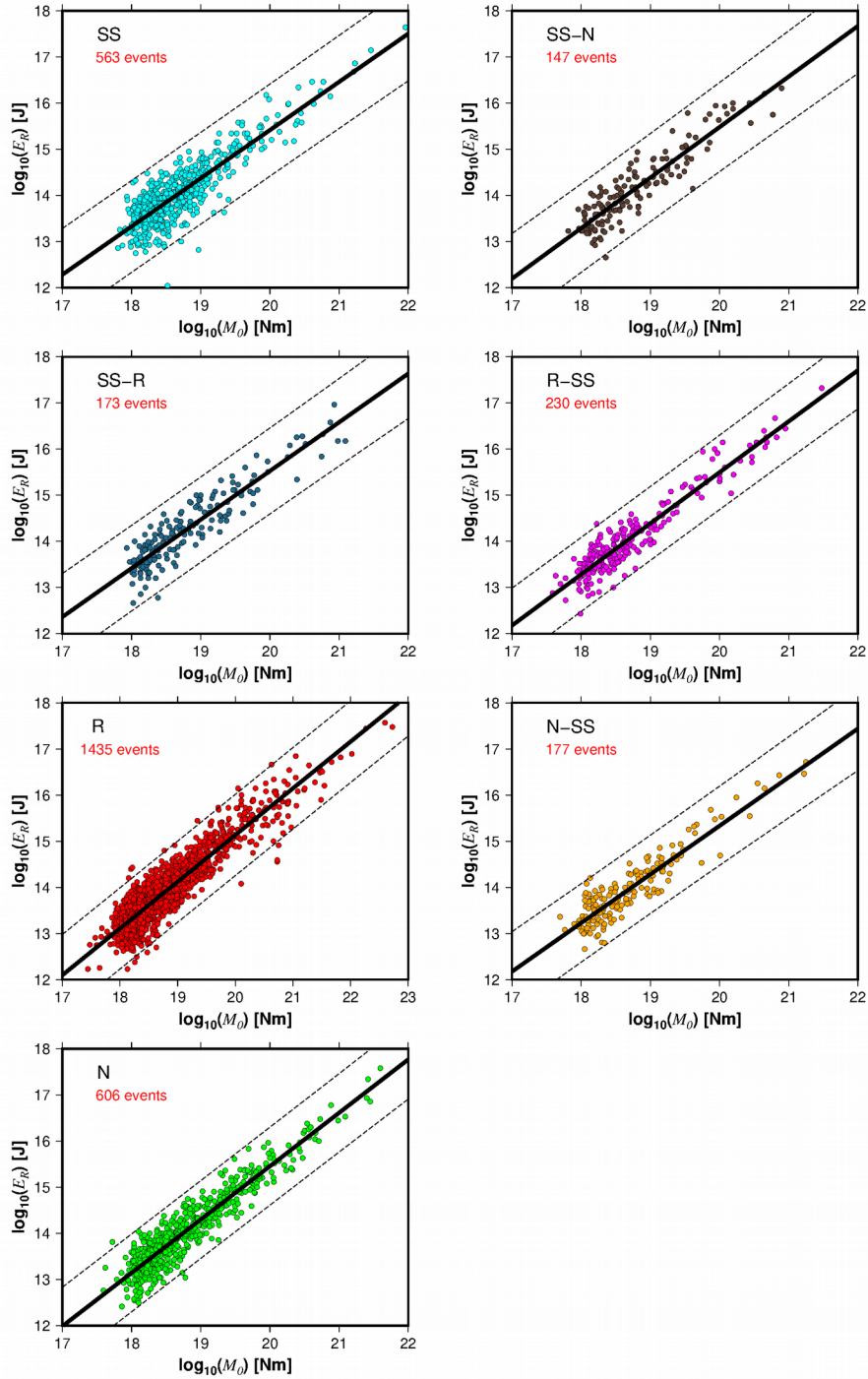
561





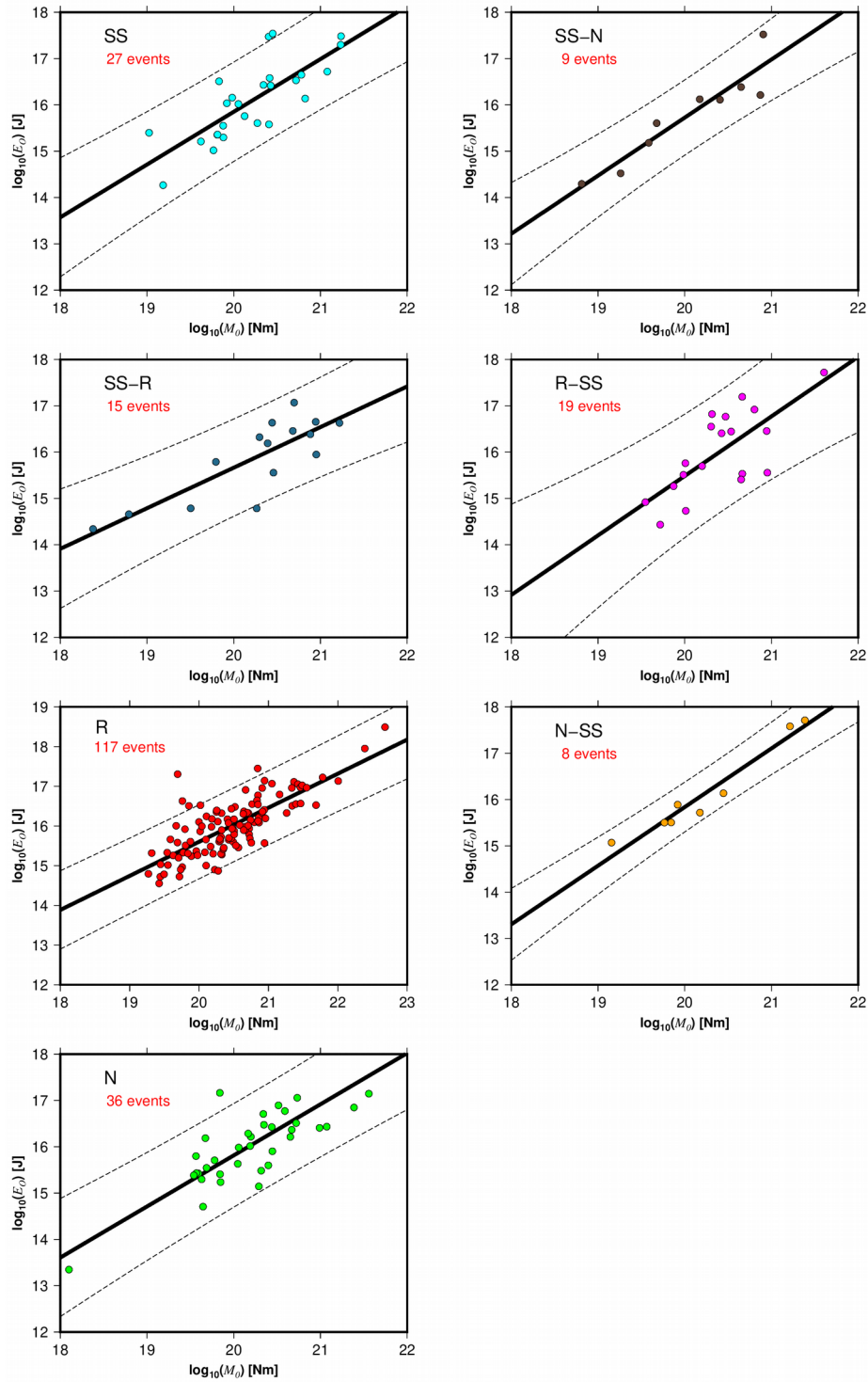
562

563 **Figure 2.** Hypocenter location and rupture type classification of earthquakes with reported radiated  
 564 seismic energy ( $E_R$ ) (upper panel). Hypocenter location and rupture type classification of earthquakes  
 565 with a finite-fault model used to calculate the radiated seismic energy ( $E_R$ ) (lower panel). R, reverse; R-  
 566 SS, reverse-strike-slip; SS, strike-slip; SS-R, strike-slip-reverse; SS-N, strike-slip-normal; N, normal;  
 567 and N-SS, normal-strike-slip.



568

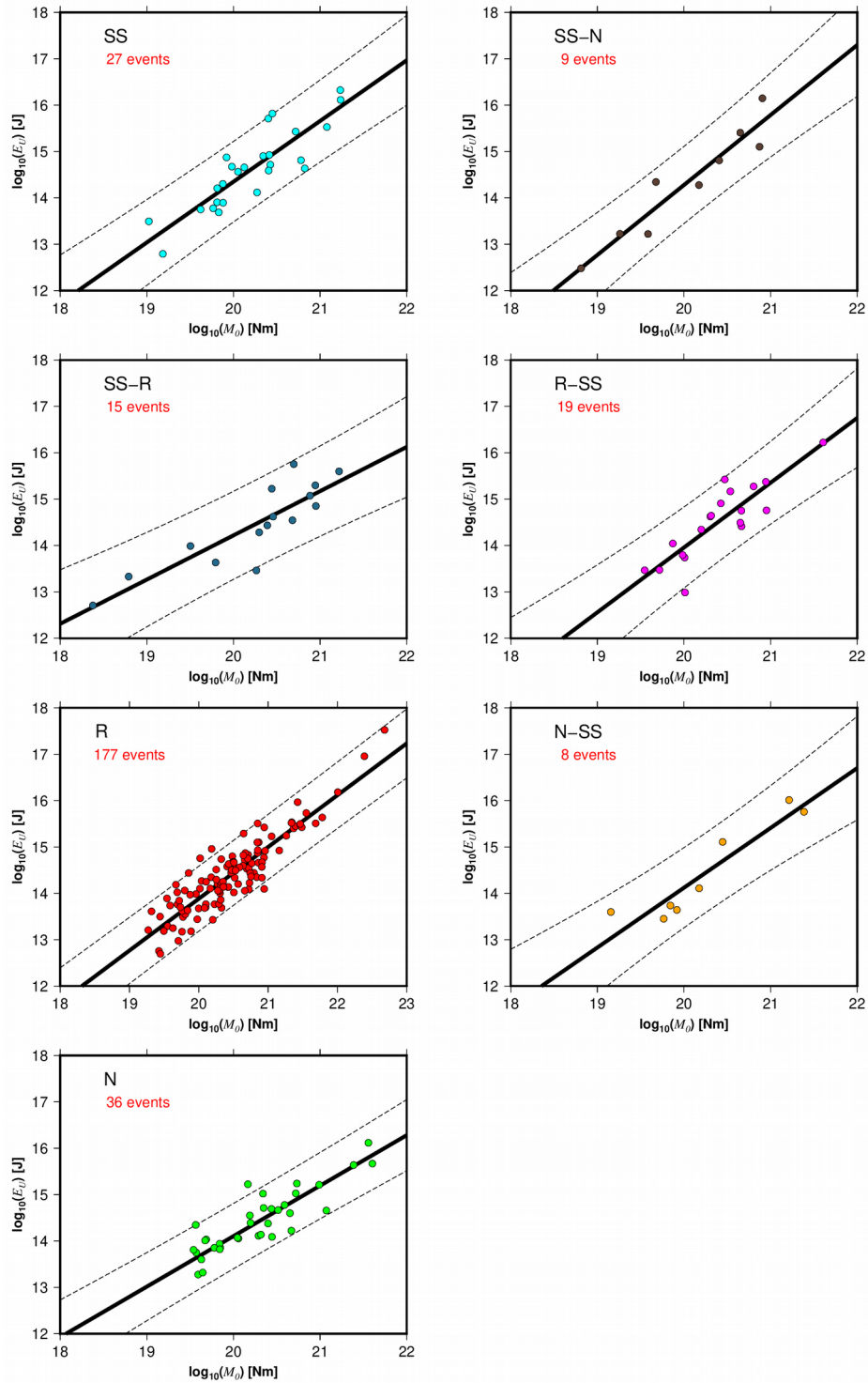
569 **Figure 3.** The radiated seismic energy ( $E_R$ ) as a function of the seismic moment ( $M_0$ ) for the different  
 570 rupture types. The solid black lines represent the best fit, and the dashed lines indicate the 95%  
 571 confidence interval about the regression lines.



572

573 **Figure 4.** The overdamped dynamics approximation of the radiated energy ( $E_0$ ) as a function of the  
 574 seismic moment ( $M_0$ ) for the different rupture types. The solid black lines represent the best fit, and the  
 575 dashed lines indicate the 95% confidence interval about the regression lines.

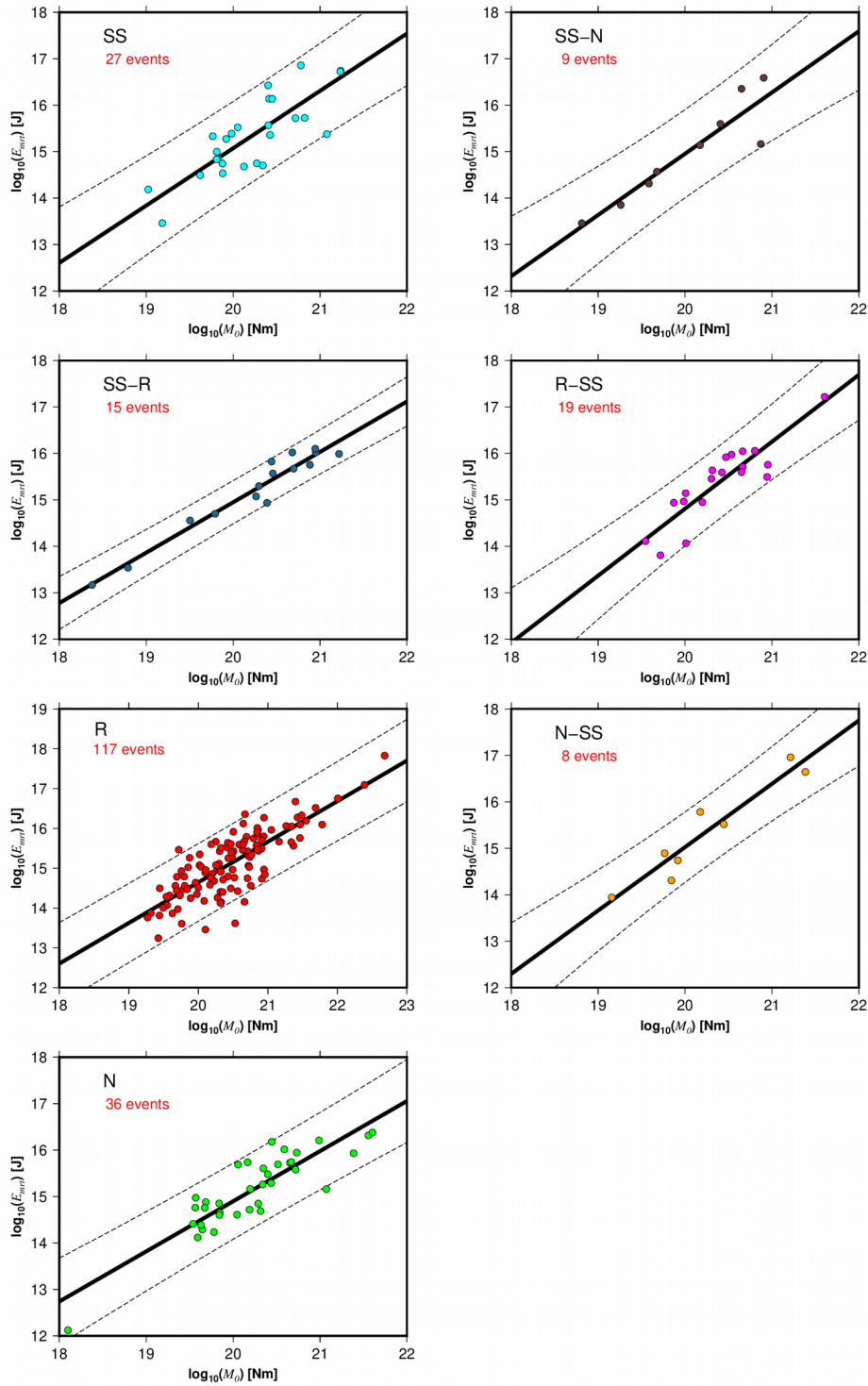




576

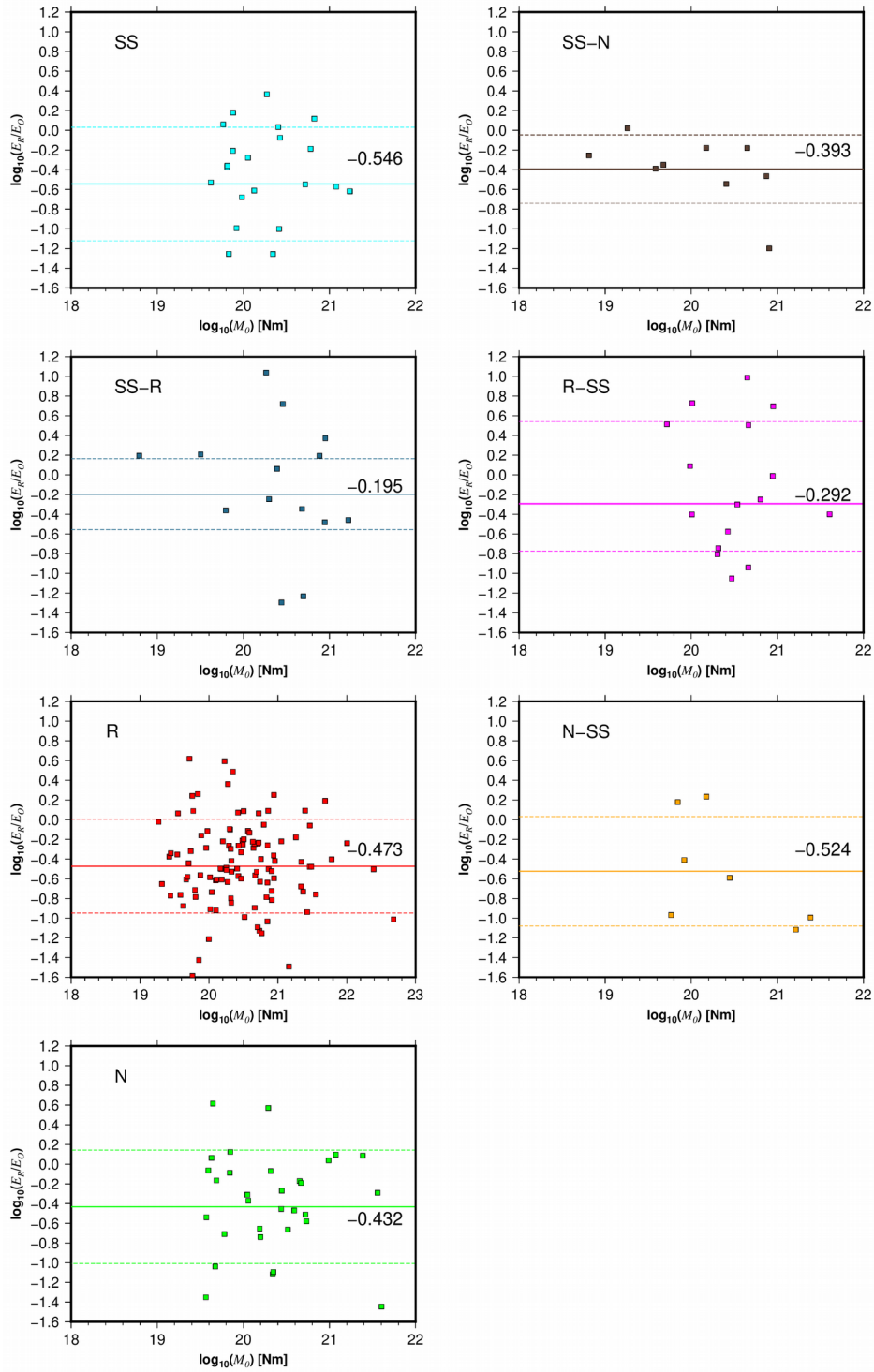
577 **Figure 5.** The energy obtained from the averaged finite-fault model ( $E_U$ ) as a function of the seismic  
 578 moment ( $M_0$ ) for the different rupture types. The solid black lines represent the best fit, and the dashed  
 579 lines indicate the 95% confidence interval about the regression lines.





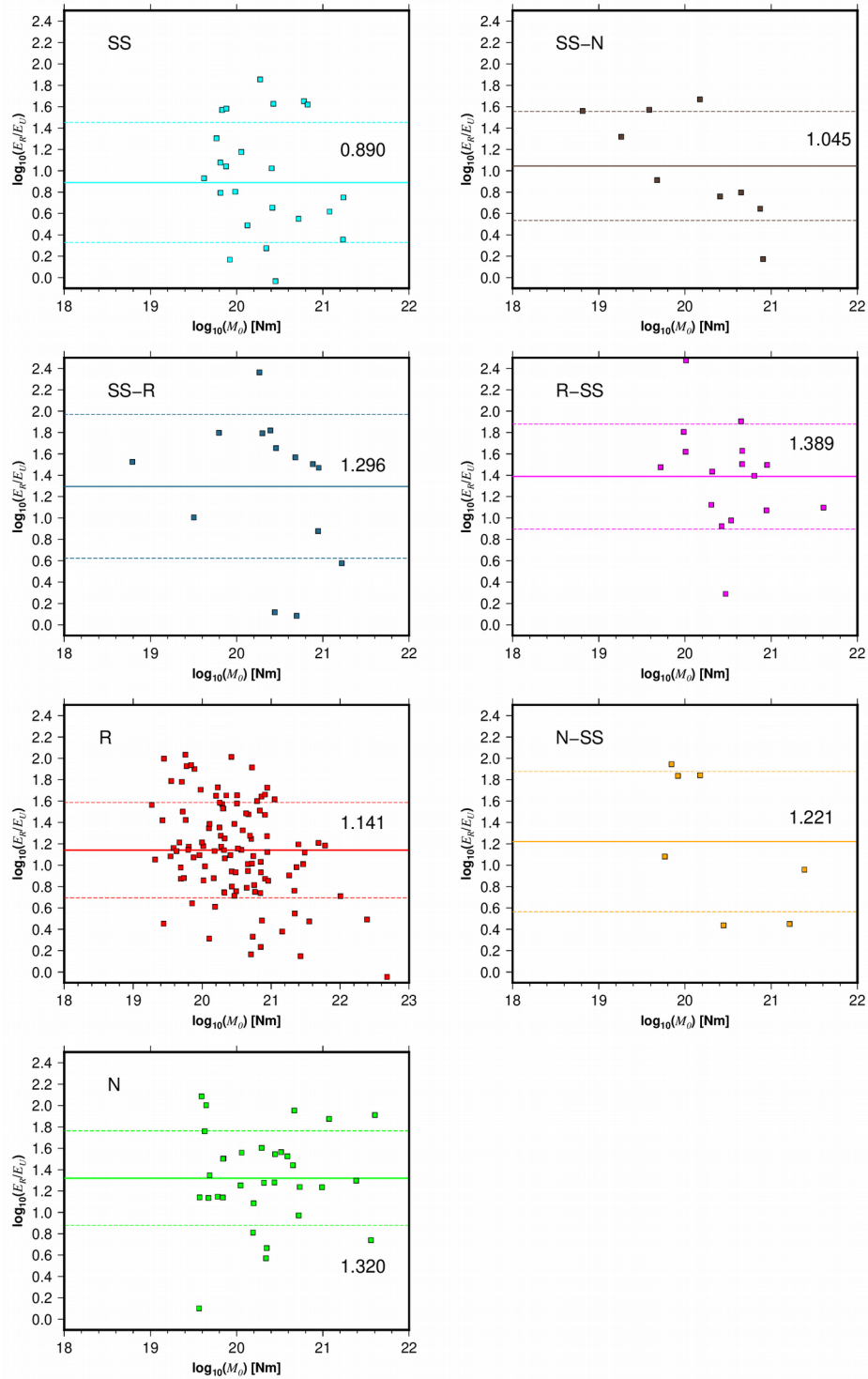
580

581 **Figure 6.** The radiated seismic energy based on moment rate functions ( $E_{rmt}$ ) versus seismic moment  
 582 ( $M_0$ ) for the different rupture types. The solid black lines represent the best fit, and the dashed lines  
 583 indicate the 95% confidence interval about the regression lines.



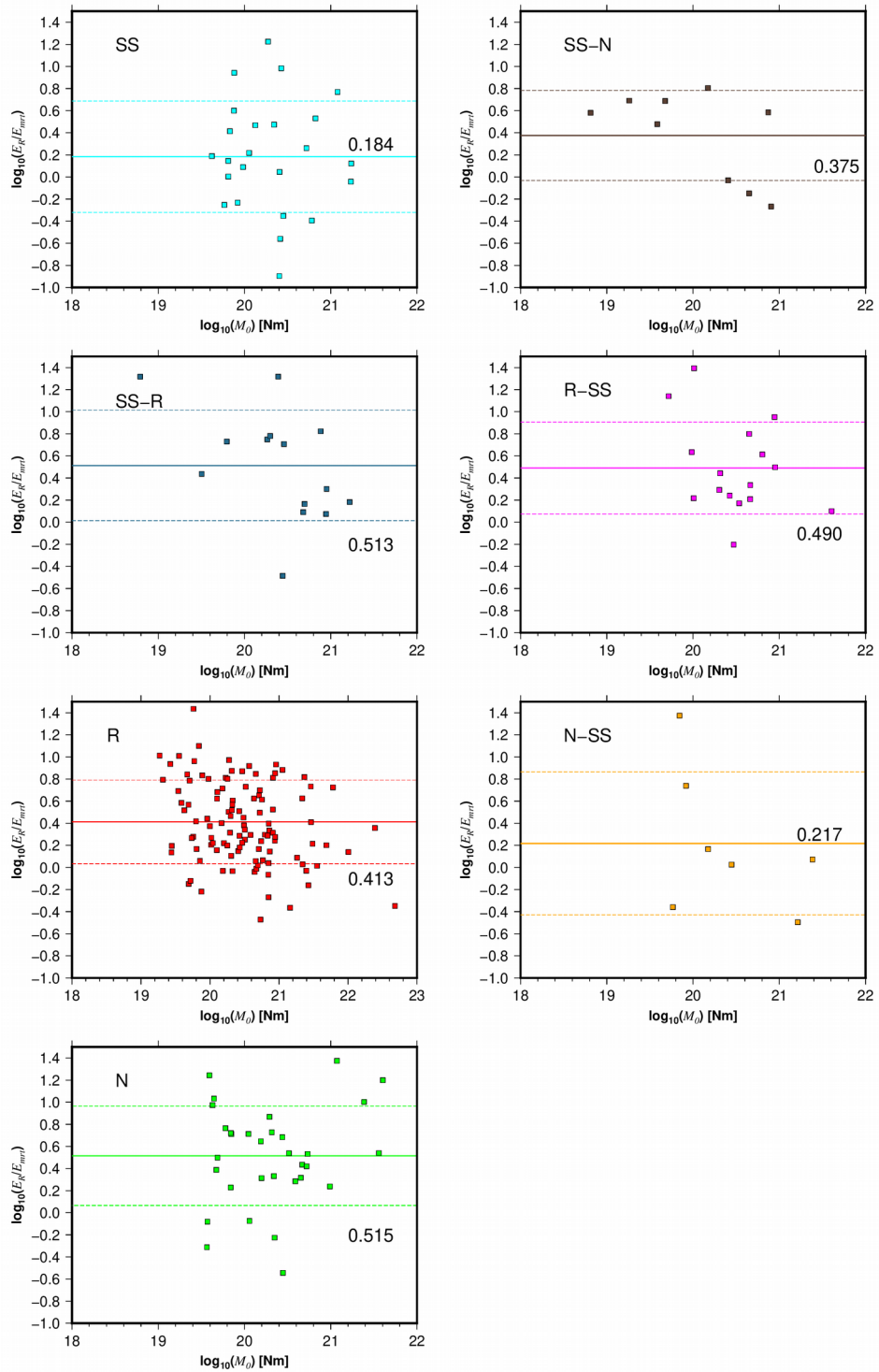
584

585 **Figure 7.** Comparison between radiated seismic energy based on velocity flux integration ( $E_R$ ) and  
 586 overdamped ( $E_O$ ) energy estimations. Lines represent the mean values (continuous) of different rupture  
 587 types and their standard deviation (dashed).



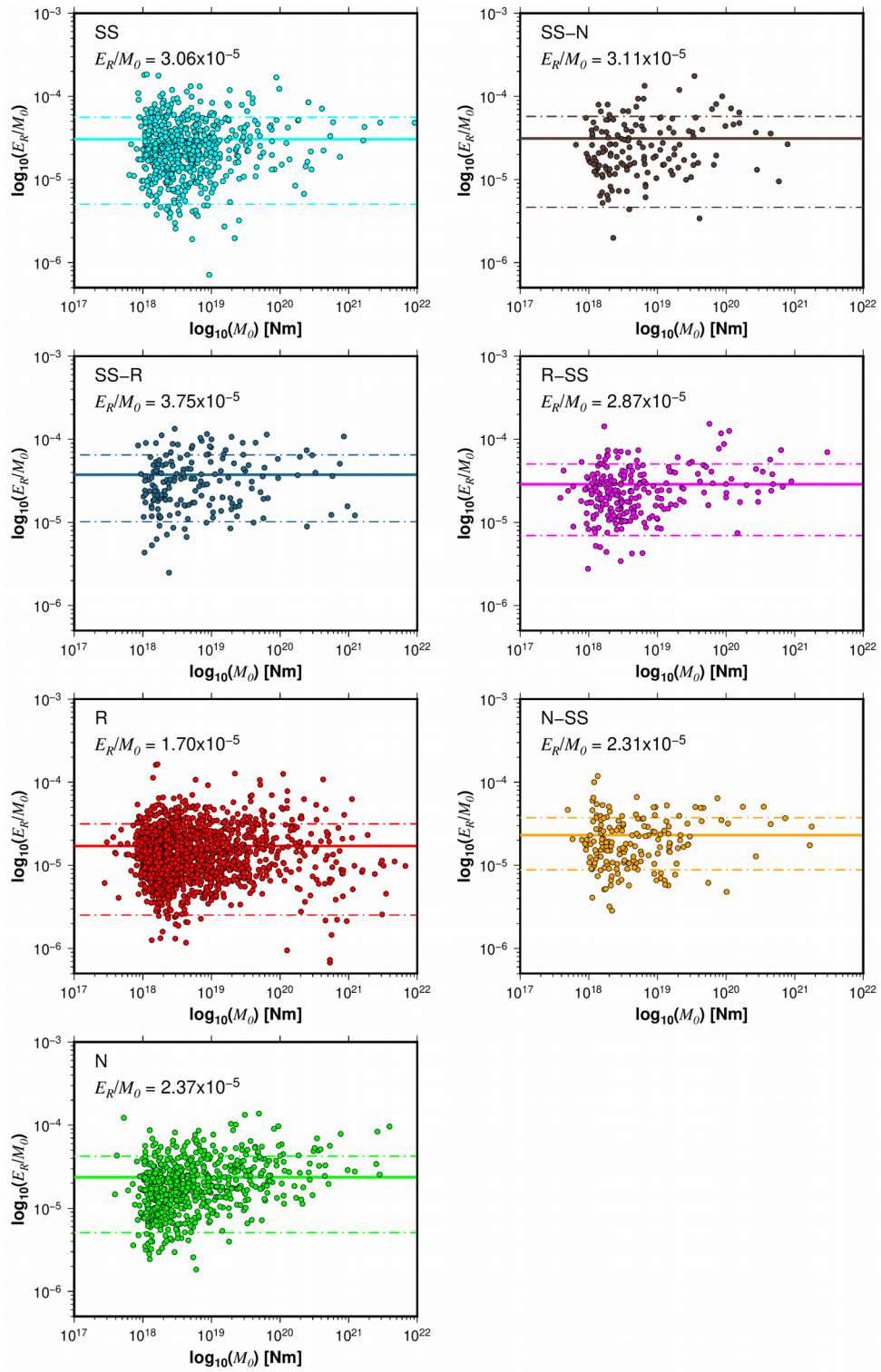
588

589 **Figure 8.** Comparison between the ratio of radiated seismic energy based on velocity flux integration  
 590 ( $E_R$ ) and averaged finite-fault model energy ( $E_V$ ) estimations as a function of seismic moment. Lines  
 591 represent the mean values (continuous) of different rupture types and their standard deviation (dashed).



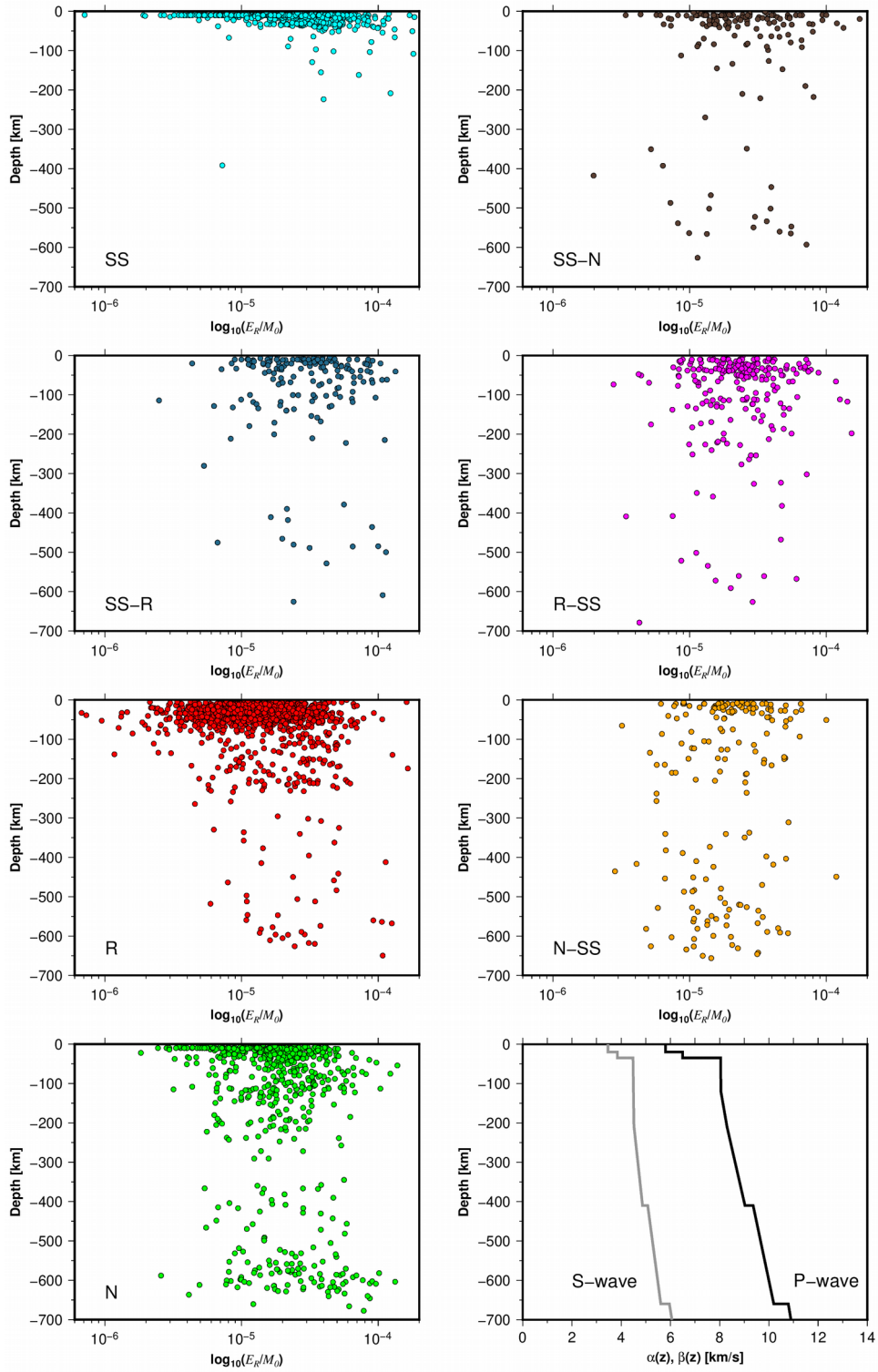
592

593 **Figure 9.** Comparison between the ratio of radiated seismic energy based on velocity flux integration  
 594 ( $E_R$ ) and moment rate ( $E_{mrt}$ ) energy estimations as a function of seismic moment. Lines represent the  
 595 mean values (continuous) of different rupture types and their standard deviation (dashed).



596

597 **Figure 10.** The estimated energy-to-moment ratios plotted as a function of the seismic moment for all  
 598 the rupture types. The solid and dashed lines show the mean value and standard deviations,  
 599 respectively.



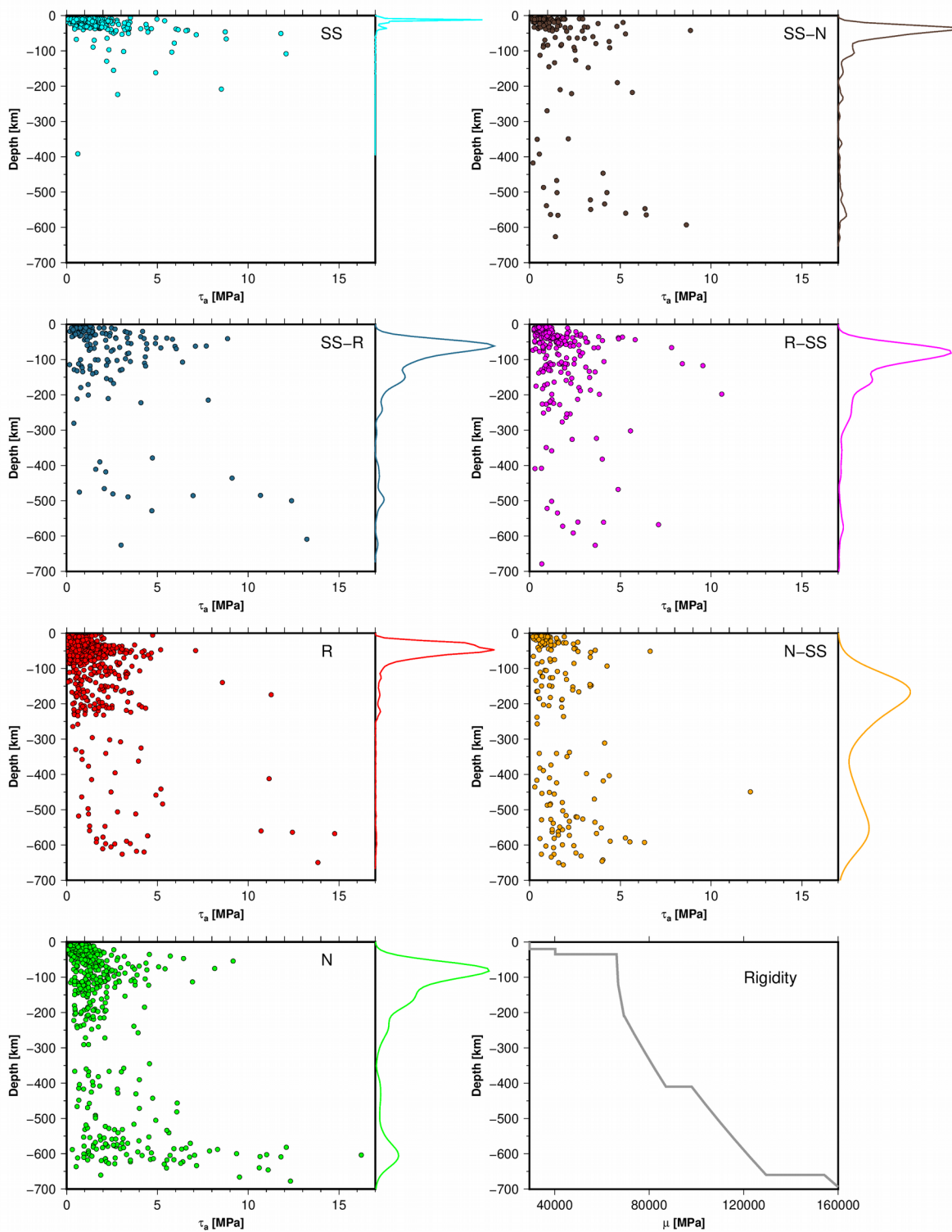
600

601 **Figure 11.** Energy-to-moment ratios with respect to depth for all rupture types. Lower right panel

602 shows the ak135-F global velocity model.

603





604

605 **Figure 12.** Apparent stress ( $\tau_a$ ) with respect to depth for all rupture types. Color curves are the  
 606 probability density functions (PDFs). Rigidity vs depth based on the ak135-F global velocity model  
 607 employed in the estimation of  $\tau_a$  (lower right panel).

608 **Table 1.** Regression results for the radiated seismic energy scaling relationships. The scaling relation is  
609 given by  $\log_{10} E = a \log_{10} M_0 + b$ , where  $E$  is the radiated seismic energy based on velocity flux  
610 integration ( $E_R$ ), the overdamped dynamics approximation of the radiated energy ( $E_O$ ), the energy  
611 obtained from the averaged finite-fault model ( $E_U$ ), or the energy obtained from moment rate functions  
612 ( $E_{mrt}$ ) in J,  $M_0$  is the seismic moment in Nm.  $D^2$  is the determination coefficient,  $a$  is the slope,  $Sa$  is the  
613 standard error of  $a$ ,  $b$  is the intercept, and  $Sb$  is the standard error of  $b$ .

Parameter	$a$	$Sa$	$b$	$Sb$	$D^2$	Rupture type	Method
$E_R$ [J]	1.04	0.02	-5.47	0.47	0.76	SS	Velocity flux integration
$E_R$ [J]	1.09	0.04	-6.42	0.78	0.83	SS-N	Velocity flux integration
$E_R$ [J]	1.05	0.03	-5.57	0.65	0.84	SS-R	Velocity flux integration
$E_R$ [J]	1.10	0.03	-6.62	0.48	0.89	R-SS	Velocity flux integration
$E_R$ [J]	1.01	0.01	-5.10	0.21	0.85	R	Velocity flux integration
$E_R$ [J]	1.05	0.03	-5.72	0.64	0.84	N-SS	Velocity flux integration
$E_R$ [J]	1.16	0.02	-7.67	0.33	0.87	N	Velocity flux integration
$E_O$ [J]	1.14	0.16	-6.93	3.17	0.68	SS	Finite-fault model
$E_O$ [J]	1.25	0.18	-9.35	3.67	0.87	SS-N	Finite-fault model
$E_O$ [J]	0.88	0.17	-1.86	3.39	0.68	SS-R	Finite-fault model
$E_O$ [J]	1.28	0.30	-10.21	6.18	0.51	R-SS	Finite-fault model
$E_O$ [J]	0.86	0.07	-1.57	1.38	0.59	R	Finite-fault model
$E_O$ [J]	1.27	0.13	-9.50	2.55	0.94	N-SS	Finite-fault model
$E_O$ [J]	1.10	0.14	-6.26	2.80	0.65	N	Finite-fault model
$E_U$ [J]	1.31	0.13	-11.85	2.56	0.81	SS	Finite-fault model
$E_U$ [J]	1.51	0.19	-15.92	3.76	0.90	SS-N	Finite-fault model
$E_U$ [J]	0.95	0.15	-4.86	3.06	0.75	SS-R	Finite-fault model
$E_U$ [J]	1.40	0.20	-14.00	4.05	0.74	R-SS	Finite-fault model
$E_U$ [J]	1.12	0.05	-8.44	1.03	0.81	R	Finite-fault model
$E_U$ [J]	1.29	0.20	-11.68	4.11	0.87	N-SS	Finite-fault model
$E_U$ [J]	1.09	0.09	-7.68	1.76	0.82	N	Finite-fault model
$E_{mrt}$ [J]	1.23	0.15	-9.61	2.97	0.74	SS	Moment rate function
$E_{mrt}$ [J]	1.32	0.21	-11.42	4.30	0.84	SS-N	Moment rate function
$E_{mrt}$ [J]	1.08	0.07	-6.75	1.50	0.94	SS-R	Moment rate function
$E_{mrt}$ [J]	1.44	0.18	-14.02	3.71	0.79	R-SS	Moment rate function
$E_{mrt}$ [J]	1.02	0.07	-5.76	1.44	0.65	R	Moment rate function
$E_{mrt}$ [J]	1.36	0.18	-12.25	3.61	0.91	N-SS	Moment rate function
$E_{mrt}$ [J]	1.08	0.10	-6.68	2.05	0.77	N	Moment rate function

614  
615  
616  
617  
618  
619  
620  
621



622 **Table 2.** Conversion relationships among the different types of energies.  $E_R$  is the radiated seismic  
623 energy based on velocity flux integration,  $E_O$  is the overdamped dynamics approximation of the  
624 radiated energy,  $E_U$  is the energy obtained from the averaged finite-fault model, and  $E_{mrt}$  is the energy  
625 obtained from moment rate functions.

Rupture type	Parameters	Model	$a$	$Sa$	$b$	$Sb$	$D^2$
SS	$E_R, E_O$	$\log_{10}E_R = a \log_{10}E_O + b$	0.61	0.12	5.83	1.90	0.54
SS-N	$E_R, E_O$	$\log_{10}E_R = a \log_{10}E_O + b$	0.75	0.09	3.60	1.42	0.91
SS-R	$E_R, E_O$	$\log_{10}E_R = a \log_{10}E_O + b$	0.37	0.16	9.96	2.60	0.30
N-SS	$E_R, E_O$	$\log_{10}E_R = a \log_{10}E_O + b$	0.61	0.19	5.78	3.19	0.66
N	$E_R, E_O$	$\log_{10}E_R = a \log_{10}E_O + b$	0.59	0.10	6.23	1.67	0.52
R-SS	$E_R, E_O$	$\log_{10}E_R = a \log_{10}E_O + b$	0.44	0.12	8.90	1.95	0.49
R	$E_R, E_O$	$\log_{10}E_R = a \log_{10}E_O + b$	0.70	0.06	4.27	0.91	0.59
SS	$E_R, E_U$	$\log_{10}E_R = a \log_{10}E_U + b$	0.61	0.11	6.67	1.59	0.59
SS-N	$E_R, E_U$	$\log_{10}E_R = a \log_{10}E_U + b$	0.63	0.08	6.40	1.18	0.89
SS-R	$E_R, E_U$	$\log_{10}E_R = a \log_{10}E_U + b$	0.35	0.17	10.73	2.43	0.28
N-SS	$E_R, E_U$	$\log_{10}E_R = a \log_{10}E_U + b$	0.54	0.18	7.96	2.65	0.63
N	$E_R, E_U$	$\log_{10}E_R = a \log_{10}E_U + b$	0.78	0.11	4.50	1.62	0.61
R-SS	$E_R, E_U$	$\log_{10}E_R = a \log_{10}E_U + b$	0.56	0.11	7.82	1.58	0.66
R	$E_R, E_U$	$\log_{10}E_R = a \log_{10}E_U + b$	0.69	0.04	5.67	0.63	0.69
SS	$E_R, E_{mrt}$	$\log_{10}E_R = a \log_{10}E_{mrt} + b$	0.66	0.10	5.49	1.56	0.65
SS-N	$E_R, E_{mrt}$	$\log_{10}E_R = a \log_{10}E_{mrt} + b$	0.70	0.09	4.93	1.32	0.90
SS-R	$E_R, E_{mrt}$	$\log_{10}E_R = a \log_{10}E_{mrt} + b$	0.52	0.14	7.84	2.16	0.54
N-SS	$E_R, E_{mrt}$	$\log_{10}E_R = a \log_{10}E_{mrt} + b$	0.55	0.21	7.23	3.30	0.57
N	$E_R, E_{mrt}$	$\log_{10}E_R = a \log_{10}E_{mrt} + b$	0.78	0.11	3.81	1.79	0.60
R-SS	$E_R, E_{mrt}$	$\log_{10}E_R = a \log_{10}E_{mrt} + b$	0.62	0.10	6.41	1.50	0.75
R	$E_R, E_{mrt}$	$\log_{10}E_R = a \log_{10}E_{mrt} + b$	0.73	0.04	4.54	0.55	0.78

626  
627  
628  
629  
630  
631  
632  
633  
634  
635  
636  
637  
638  
639  
640  
641  
642  
643

644 **Table 3.** Estimations of average apparent stress ( $\tau_\alpha$ ) for different faulting types based on the velocity  
645 flux integration method.  $\tau_\alpha$  is calculated with the following model:  $\log_{10}E_R = \log_{10} M_0 + b$ , where  $\tau_\alpha = \mu$   
646  $10^b$ . We assume  $\mu = \bar{\mu}$  as the average rigidity in a specific depth interval of 30 km.  $\tau_\alpha^1$  and  $\tau_\alpha^2$  are the  
647 95% the upper and lower confidence intervals for the mean. 3 and 4 indicate  $\tau_\alpha$  results from Choy and  
648 Boatwright (1995) and Pérez-Campos and Beroza (2001), respectively (bottom lines).

Depth [km]	$\bar{\mu}$ [MPa]	$\tau_\alpha$ [MPa]							$\tau_\alpha^1$ [MPa]							$\tau_\alpha^2$ [MPa]						
		SS	SS-N	SS-R	N-SS	N	R-SS	R	SS	SS-N	SS-R	N-SS	N	R-SS	R	SS	SS-N	SS-R	N-SS	N	R-SS	R
$0 \leq z \leq 30$	$3.48 \times 10^4$	0.72	0.75	0.90	0.72	0.50	0.79	0.43	3.51	3.31	3.41	2.20	1.91	2.34	1.40	0.15	0.17	0.24	0.24	0.13	0.26	0.13
$30 < z \leq 60$	$5.33 \times 10^4$	1.95	1.49	2.47	1.33	1.03	1.29	0.68	6.76	8.65	9.79	6.55	4.57	4.92	2.82	0.56	0.26	0.62	0.27	0.23	0.39	0.16
$60 < z \leq 90$	$6.65 \times 10^4$	1.75		3.08	1.58		1.37	0.73	6.75		12.21	6.85		9.55	4.33	0.45		0.78	0.37		0.19	0.12
$90 < z \leq 120$	$6.67 \times 10^4$	1.88			1.49		1.96	1.45	13.59			5.95		8.55	7.08	0.26		0.37		0.45	0.30	
$120 < z \leq 150$	$6.73 \times 10^4$	1.22		1.15	1.13	1.38	0.90	5.55			6.57	3.76	5.43	7.86	0.27		0.20	0.34	0.35	0.10		
$150 < z \leq 180$	$6.81 \times 10^4$	1.55			1.38		3.93			7.79		0.61		0.24								
$180 < z \leq 210$	$6.90 \times 10^4$	1.09			1.35		4.07			5.52		0.29		0.33								
$210 < z \leq 240$	$7.07 \times 10^4$	1.19			1.34		5.17			6.04		0.27		0.30								
$540 < z \leq 570$	$1.16 \times 10^5$	2.39			7.61		0.75															
$570 < z \leq 600$	$1.19 \times 10^5$	2.88			14.88		0.56															
$600 < z \leq 630$	$1.23 \times 10^5$	3.33			18.76		0.59															
	$3.00 \times 10^5$	3.55 <sup>3</sup>		0.48 <sup>3</sup>		0.32 <sup>3</sup>	20.69 <sup>3</sup>	4.16 <sup>3</sup>		2.54 <sup>3</sup>	0.61 <sup>3</sup>		0.05 <sup>3</sup>		0.04 <sup>4</sup>							
	$3.00 \times 10^5$	0.70 <sup>4</sup>		0.25 <sup>4</sup>		0.15 <sup>4</sup>	1.01 <sup>4</sup>	0.30 <sup>4</sup>		0.19 <sup>4</sup>	0.49 <sup>4</sup>		0.21 <sup>4</sup>		0.12 <sup>4</sup>							

649

650

651 **Table 4.** Estimations of average apparent stress ( $\tau_\alpha$ ) for different faulting types based on slip  
652 distributions ( $E_{mt}$ ,  $E_U$ , and  $E_O$ ).  $\tau_\alpha$  is calculated with the following model:  $\log_{10}E_R = \log_{10} M_0 + b$ , where  $\tau_\alpha$   
653  $= \mu 10^b$ . We assume  $\mu = \bar{\mu}$  as the average rigidity in a specific depth interval of 30 km.  $\tau_\alpha^1$  and  $\tau_\alpha^2$  are  
654 the 95% the upper and lower confidence intervals for the mean. 3 and 4 indicate  $\tau_\alpha$  results from Choy  
655 and Boatwright (1995) and Pérez-Campos and Beroza (2001), respectively (bottom lines).

Depth [km]	$\bar{\mu}$ [MPa]	$\tau_\alpha$ [MPa]							$\tau_\alpha^1$ [MPa]							$\tau_\alpha^2$ [MPa]						
		SS	SS-N	SS-R	N-SS	N	R-SS	R	SS	SS-N	SS-R	N-SS	N	R-SS	R	SS	SS-N	SS-R	N-SS	N	R-SS	R
$E_{mt}$																						
$0 \leq z \leq 30$	$3.48 \times 10^4$	0.52	0.33		0.31		0.16	5.72	1.36		2.10		1.47	0.05	0.08		0.05		0.02			
$30 < z \leq 60$	$5.33 \times 10^4$	0.24		2.10		2.28																
$E_U$																						
$0 \leq z \leq 30$	$3.48 \times 10^4$	2.78	1.41		2.59		1.50	32.77	23.19		21.79		19.92	0.24	0.08		0.10		0.11			
$30 < z \leq 60$	$5.33 \times 10^4$	2.31		30.51																		
$E_O$																						
$0 \leq z \leq 30$	$3.48 \times 10^4$	0.10	0.04		0.04		0.03	0.91	0.51		0.24		0.17	0.01	0.01		0.09		0.005			
$30 < z \leq 60$	$5.33 \times 10^4$	0.04		0.04		0.04																
	$3.00 \times 10^5$	3.55 <sup>3</sup>		0.48 <sup>3</sup>		0.32 <sup>3</sup>	20.69 <sup>3</sup>	4.16 <sup>3</sup>		2.54 <sup>3</sup>	0.61 <sup>3</sup>		0.05 <sup>3</sup>		0.04 <sup>4</sup>							
	$3.00 \times 10^5$	0.70 <sup>4</sup>		0.25 <sup>4</sup>		0.15 <sup>4</sup>	1.01 <sup>4</sup>	0.30 <sup>4</sup>		0.19 <sup>4</sup>	0.49 <sup>4</sup>		0.21 <sup>4</sup>		0.12 <sup>4</sup>							

656